Biogeosciences Discuss., 10, 5841–5888, 2013
www.biogeosciences-discuss.net/10/5841/2013/
doi:10.5194/bgd-10-5841-2013

Biogeosciences Discussions
Open Access

Indian Ocean Dipole and El Niño/Southern Oscillation impacts on regional chlorophyll anomalies in the Indian Ocean

J. C. Currie[1], M. Lengaigne[2], J. Vialard[2], D. M. Kaplan[3], O. Aumont[4], S. W. A. Naqvi[5], and O. Maury[3,6]

[1]Biological Sciences Department, Marine Research Institute, University of Cape Town, South Africa
[2]Institut de Recherche pour le Développement, Laboratoire d'Océanographie et du Climat: Expérimentation et Approches Numériques, UMR 7617, Université Pierre et Marie Curie, Paris, France
[3]Institut de Recherche pour le Développement, UMR 212 EME (IRD, IFREMER, Université Montpellier II), Sète cedex, France
[4]Institut de Recherche pour le Développement, Laboratoire de Physique des Océans, UMR 6523, Brest, France
[5]CSIR-National Institute of Oceanography, Dona Paula, Goa, India
[6]Department of Oceanography, Marine Research Institute, University of Cape Town, South Africa

Received: 25 February 2013 – Accepted: 28 February 2013 – Published: 26 March 2013

Correspondence to: J. C. Currie (jockcurrie@gmail.com)

Published by Copernicus Publications on behalf of the European Geosciences Union.

Abstract

The Indian Ocean Dipole (IOD) and the El Niño-Southern Oscillation (ENSO) frequently co-occur, driving significant interannual changes within the Indian Ocean. We use a four-decade hindcast from a coupled bio-physical ocean general circulation model, to disentangle patterns of chlorophyll anomalies driven by these two climate modes. Comparisons with remotely-sensed records show that the simulation competently reproduces the chlorophyll seasonal cycle, as well as open-ocean anomalies during the 1997–1998 ENSO and IOD event. Results show that anomalous surface and euphotic-layer chlorophyll blooms in the eastern equatorial Indian Ocean in fall, and southern Bay of Bengal in winter, are primarily related to IOD forcing. IOD depresses integrated chlorophyll in the 5° S–10° S thermocline ridge region, even though the signal is negligible in surface chlorophyll. A previously-unreported negative influence of IOD on chlorophyll concentrations is also shown in a region around the southern tip of India. The only investigated region where ENSO has a greater influence on chlorophyll than does IOD, is in the Somalia upwelling region, where it causes a decrease in fall and winter chlorophyll by reducing local upwelling winds. Lastly, we show that the chlorophyll impact of climate indices is frequently asymmetric, with a general tendency for larger positive than negative chlorophyll anomalies. ENSO and IOD cause significant and predictable regional re-organisation of phytoplankton productivity via their influence on near-surface oceanography. Resolving the details of these effects should improve our understanding, and eventually gain predictability, of interannual changes in Indian Ocean productivity, fisheries, ecosystems and carbon budgets.

1 Introduction

The El Niño-Southern Oscillation (ENSO) is well-known as the dominant mode of interannual climate variability that develops from air-sea interactions in the tropical Pacific, but affects weather patterns globally (McPhaden et al., 2006). During an El Niño,

BGD
10, 5841–5888, 2013

air-sea interactions promote the growth of positive sea surface temperature (SST) and sea level anomalies in the central and eastern Pacific and corresponding negative anomalies in the western Pacific. Changes in thermocline depth and surface ocean dynamics and thermodynamics are driven by anomalous atmospheric conditions, most notably westerly surface winds in the central and western ocean (Wang and Fiedler, 2006). Sea surface temperature (SST) expression of ENSO events generally peak between November and January (Trenberth, 1997). Teleconnections associated with El Niño result in an overall warming of the Indian Ocean (Klein et al., 1999; Murtugudde and Busalacchi, 1999; Xie et al., 2009), due to changing cloud cover and wind patterns that relate to changes in ascending and descending branches of the Walker circulation (Du et al., 2009; Reason et al., 2000; Venzke et al., 2000). In turn, such physical perturbations can affect the biology in local and distant oceans (Ménard et al., 2007; Spencer et al., 2000; Vinueza et al., 2006). Applying empirical orthogonal function (EOF) analyses to four years of global SeaWiFS data, which provide an estimate of surface phytoplankton biomass, Yoder and Kennelly (2003) identified two interannual modes of variability in surface chlorophyll, both of which they ascribed to ENSO control.

Whereas the Indian Ocean was previously considered to be largely passive, with interannual variations arising from the remote forcing of ENSO, it was shown in the late 1990s to exhibit its own mode of interannual variability (Murtugudde and Busalacchi, 1999; Saji et al., 1999; Webster et al., 1999), which impacts both local and remote regions (Izumo et al., 2010; Yamagata et al., 2004). Commonly referred to as the Indian Ocean Dipole (IOD) mode, even though contention exists over whether it should be referred to as a "dipole" (Baquero-Bernal et al., 2002; Hastenrath, 2002), it is associated with anomalous easterly winds in the central Indian Ocean and cold SST anomalies off the south and west coasts of Java and Sumatra. These two anomalies enhance each other in a positive feedback loop (Reverdin et al., 1986; Webster et al., 1999) similar to the Bjerknes feedback critical to ENSO events (Bjerknes, 1969). The anomalous easterly winds raise the thermocline in the eastern part of the basin and, together with off-equatorial Rossby wave responses, deepen the thermocline and warm the SST in

BGD
10, 5841–5888, 2013

the western Indian Ocean, resulting in characteristic zonal anomaly patterns in sea level height, as well as surface and subsurface temperature structures (e.g. Feng and Meyers, 2003; Murtugudde et al., 2004; Rao et al., 2002). Subsurface temperature anomalies typically initiate earlier and persist longer than the surface temperature signals (Horii et al., 2008). Negative IOD events feature opposite anomalies over similar regions (Meyers et al., 2007; Vinayachandran et al., 2002). Like ENSO, IOD events are phase-locked to the seasonal cycle and develop during boreal spring, peak in about October, and decay by the end of the calendar year. IOD events are commonly triggered by El Niño events, but can also occur independently (Annamalai et al., 2003; Meyers et al., 2007; Song et al., 2007; Yamagata et al., 2004).

Compared to the impacts on the physical structure of the Indian Ocean, the biological consequences of IOD events have received far less attention, despite their potential importance to ecosystems, fishery resources and carbon sequestration. After the launch of SeaWiFS and with recent progression of coupled bio-physical ocean models, the fields required to investigate seasonal and interannual variability at basin scales have become increasingly accessible (e.g. Rodgers et al., 2008; Wiggert et al., 2005, 2006, 2009; Yoder and Kennelly, 2003). Satellite coverage of chlorophyll concentrations has allowed investigation of the most recent ENSO/IOD events (e.g. Iskandar et al., 2009; Murtugudde et al., 1999; Wiggert et al., 2009). The intense 1997 positive IOD/El Niño event was characterized by a strong phytoplankton bloom in the eastern equatorial Indian ocean; an area which is normally characterized by low productivity (Murtugudde et al., 1999; Susanto and Marra, 2005). The upwelling of cool, nutrient-rich water and associated biological productivity had a detrimental impact on coral reefs in a large area off the coast of Indonesia (Abram et al., 2003, 2004; van Woesik, 2004). Other documented impacts of the 1997 event included a decrease of surface chlorophyll in the Arabian Sea (Sarma, 2006) attributed to anomalous northeasterly winds, as well as a bloom in the southeastern Bay of Bengal, owing to anomalous Ekman pumping in this region (Vinayachandran and Mathew, 2003). Although similar blooms developed in the eastern Indian Ocean during the 2006 IOD (Iskandar et al., 2009), Wiggert et al. (2009)

BGD
10, 5841–5888, 2013

showed that the biological responses to the 1997 event were of greater intensity, with more persistent and stronger positive anomalies spreading further west than in 2006, due to a reversal (as opposed to weakening) of the Wyrtki Jet in the boreal fall Intermonsoon. In addition their results showed that the bloom in the southeastern Bay of Bengal and the low chlorophyll anomaly in the Arabian Sea observed during 1997 developed only weakly during the less severe 2006 event.

Wiggert et al. (2009) made use of a remote sensing-based algorithm to make a first assessment of basin-wide primary production (NPP) anomalies caused by the 1997 and 2006 IOD/El Niño events. These events appeared to have had a minimal effect on the net NPP averaged over the event periods and entire Indian Ocean, due to compensating responses among different regions. There is however a profound redistribution of the carbon uptake, with a large NPP increase in the eastern Indian Ocean, roughly balanced by a decrease in western regions. While the two events did not significantly impact surface chlorophyll in the southwestern Indian Ocean, the region did exhibit negative NPP anomalies, due to anomalously deep thermocline depths (Wiggert et al., 2009). NPP anomalies varied considerably, depending on the event considered: Positive NPP anomalies in the eastern Indian Ocean varied between 45 % and 13 %; negative anomalies in the southwestern Indian Ocean varied between −20 % and −8 %; while the Arabian Sea experienced NPP changes of −9 % and +15 % during the 1997 and 2006 events, respectively. These contrasts reveal the changing nature of biological impacts among different events.

Although SeaWiFS now provides over a decade of data at high spatial and temporal resolution, this period is still restrictive in addressing interannual or long-term changes. Only two clear positive IODs have developed during the SeaWiFS era, which represents a limited sample size and does not allow investigation of the full spectrum of possible IOD-ENSO configurations (e.g. Meyers et al., 2007; Song et al., 2008). Moreover, problems with remotely sensed chlorophyll in some oligotrophic regions have been noted (Claustre et al., 2002; Dandonneau et al., 2003) and sensors potentially miss a proportion of depth-integrated chlorophyll when chlorophyll maxima are deeper

BGD
10, 5841–5888, 2013

than the first attenuation depth or "penetration depth" (~20 m; Gordon and McCluney, 1975). Fortunately, longer-term biogeochemical and biological hindcasts from coupled bio-physical models are increasingly filling subsurface processes not captured by satellites, and are resolving seasonal and interannual variability to an ever-improving degree (e.g. Koné et al., 2009; Maury, 2010; Rodgers et al., 2008; Wiggert et al., 2006). Here we make use of a four-decade hindcast from the coupled bio-physical general circulation model, NEMO-PISCES, to assess the respective contributions of ENSO and IOD to interannual surface and vertically-integrated chlorophyll anomalies in the Indian Ocean. Focusing predominantly on the biological response, we also assess responses in SST, thermocline depth and surface winds to explore the processes driving the variability in chlorophyll. An improved understanding of such dynamics should aid constructive hypotheses about, and interpretations of, ecosystem links to climate variability and thereby contribute towards attaining predictability of impacts from similar events in future.

The paper is structured as follows: Sect. 2 describes the data and methods used. A brief comparison between the modelled surface chlorophyll and SeaWiFS outputs is provided for the Indian Ocean in Sect. 3. Section 4 describes the influences of IOD and ENSO on thermal and chlorophyll responses in surface waters of the Indian Ocean. Section 5 summarizes our main findings and discusses them in context of previous literature.

2 Data and methods

2.1 Observed datasets

Chlorophyll *a* (chl *a*) concentrations were obtained from the European Space Agency's GlobColour project. We used a remotely sensed level 3 (binned and mapped) 1° and monthly resolution chl *a* dataset, which is derived using standard case 1 water algorithms (Morel and Maritorena, 2001; O'Reilly et al., 1998). This dataset is a merged

BGD
10, 5841–5888, 2013

product from three sensors (SeaWiFS, MERIS, and MODIS-Aqua), which has approximately twice the mean global coverage and lower uncertainties in retrieved variables compared to data from individual sensors (Maritorena et al., 2010). While small systematic differences exist among the products of individual sensors, the large-scale chl *a* distributions produced by these major ocean colour missions are consistent over a wide range of conditions (Djavidnia et al., 2010; Morel et al., 2007).

2.2 Ocean model and forcing datasets

The particular ocean and coupled biogeochemical model simulation that is used in this paper has been described in Koné et al. (2009), so we include only its main features here. The ocean configuration was built from the OPA (Ocean PArallelise) version 8.2 ocean model (Madec et al., 1998), coupled to the dynamic-thermodynamic Louvain-la-Neuve sea ice model (LIM; see Timmermann et al., 2005). This 0.5° configuration (known as ORCA05-LIM; cell size ~ 50 km in the tropics) has 30 vertical levels, of which 20 are concentrated in the upper 500 m as their thickness varies from 10 m near the surface, to 500 m at depth. Density is computed from potential temperature, salinity and pressure using the equation of state by Jackett and Mcdougall (1995). Vertical mixing is parameterized from a turbulence closure scheme based on a prognostic vertical turbulent kinetic equation, which has been shown to perform well in the tropics (Blanke and Delecluse, 1993). Lateral mixing acts along isopycnal surfaces, with a Laplacian operator and 200 $m^2 s^{-1}$ constant isopycnal diffusion coefficient (Lengaigne et al., 2003). Shortwave fluxes penetrate into the ocean based on a single exponential profile (Paulson and Simpson, 1977), corresponding to oligotrophic water (attenuation depth of 23 m). No-slip boundary conditions are applied at the coastlines.

The OGCM has been extensively validated in uncoupled (Cravatte et al., 2007; Lengaigne et al., 2002) and coupled modes (Lengaigne et al., 2006; Lengaigne and Vecchi, 2010) with various forcing strategies. It accurately simulates equatorial dynamics and basin wide structures of currents, sea level and temperature in the tropics and has provided useful insight into interannual variations of heat content in the Pacific

BGD
10, 5841–5888, 2013

(Lengaigne et al., 2012), as well as of sea level (Nidheesh et al., 2012) and mixed layer depth (De Boyer Montégut et al., 2007; Keerthi et al., 2012) in the Indian Ocean.

The ocean/sea-ice model was coupled with the Pelagic Interaction Scheme for Carbon and Ecosystem Studies (PISCES) biogeochemical model (Aumont et al., 2008; Aumont and Bopp, 2006), built to simulate biogeochemical fields in the global ocean and better understand their dynamics. A concise overview of PISCES is provided here; a full description of the model, including model parameters and brief validation of results is available in the supplementary material of Aumont and Bopp (2006). The model has 24 compartments, which include two sizes of sinking particles and four 'living' biological pools that are represented by two phytoplankton (nano-phytoplankton and diatoms) and two zooplankton (microzooplankton and mesozooplankton) size classes. Phytoplankton growth is limited by five nutrients: NO_3, NH_4, PO_4, SiO_4, and Fe. The ratios among C, N, and P are kept constant for the 'living' compartments, at values proposed by Takahashi et al. (1985). The internal Fe contents of both phytoplankton groups and Si contents of diatoms are prognostically simulated as a function of the external concentrations in nutrients and light level. Details on the Red-Green-Blue model by which light penetration profiles are calculated, are given in Lengaigne et al. (2007). The Chl/C ratio is modelled using a modified version of the photoadaptation model by Geider et al. (1998). Ratios of elements within zooplankton compartments are kept constant. Manuals for NEMO and PISCES are available online (http://www.nemo-ocean.eu/About-NEMO/Reference-manuals).

The physical model was initialized from rest with salinity and temperature climatologies of the World Ocean Atlas 2001 (Boyer et al., 2005). The biogeochemical model was initialized from outputs of the simulation described by Aumont and Bopp (2006). Surface boundary conditions of the OGCM were applied as follows: daily surface wind stresses were specified from the ERA40 re-analysis (Uppala et al., 2005). Radiation fluxes are based on the CORE v1 dataset, using the International Satellite Cloud Climatology Project radiation product (Zhang et al., 2004) available from 1984 onwards. Prior to 1984 a climatology of the radiation fluxes is imposed, which leads to better

BGD
10, 5841–5888, 2013

results than the use of reanalysis data. Precipitation is taken from the Climate Prediction Center Merged Analysis of Precipitation (CMAP; Xie and Arkin, 1997), available from 1979 onwards, while a CMAP climatology is applied before then. Evaporation and turbulent heat fluxes are computed using empirical bulk formulae by Goose (1997), which employ ERA40 daily wind speed and air temperatures, as well as climatological relative humidity fields from Trenberth et al. (1989). To avoid artificial model drift, sea surface salinity was restored towards monthly mean climatological values from the World Ocean Atlas (Boyer et al., 2005), with a time scale of 300 days for a typical 50 m-thick mixed layer. After a seven year spin-up period, a simulation was performed over the period of 1958 to 2001, providing outputs with a temporal resolution of five days.

Using the same model, Koné et al. (2009) show that Indian Ocean features of the seasonal chlorophyll cycle compare reasonably well with SeaWiFS, including the timing of bloom onsets. In addition, recognized biogeochemical provinces are reproduced in most of the Arabian Sea, Bay of Bengal and in the convergence zone south of the equator (Koné et al., 2009). In our analyses, the first three years of the simulation (1958–1960) were omitted, in order to avoid potential spin-up effects.

2.3 Methodology

The depth of the 20 °C isotherm (D20) was estimated by linear interpolation of temperature between model levels. Chlorophyll concentrations were calculated as the sum of chlorophyll from the two phytoplankton size classes (diatoms and nano-phytoplankton). Surface chlorophyll concentrations (denoted by SChl; units of $mg\,m^{-3}$) were averaged over the upper two layers (i.e. 20 m depth) for comparison with SeaWiFS. The euphotic zone was estimated from the photosynthetically available radiation (PAR) outputs, as the depth where PAR was 1 % of the surface value. The depth-integrated chlorophyll was then computed over the euphotic zone, and is referred to as integrated chlorophyll or IChl hereafter (units of $mg\,m^{-2}$).

De-seasoned anomalies for all fields were computed from monthly time-series as the remainder after removal of their mean seasonal cycle and "long-term trend"

BGD
10, 5841–5888, 2013

components by the "Seasonal Decomposition of Time Series by Loess" function (STL; Cleveland et al., 1990) in R programming language (R Development Core Team, 2011). The trend component was estimated by a degree-one polynomial fitted over a seven-year Loess window and serves to remove longer-term variability on the order of decades or greater.

To represent the interannual signal associated with IOD and ENSO, standard indices were used: in the Pacific, ENSO is commonly represented from the averaged SST anomalies over the Niño3.4 (120° W–170° W, 5° N–5° S) region during November–January (Trenberth, 1997). The Indian Ocean Dipole (IOD) was characterized by the dipole mode index (DMI; Saji et al., 1999), computed as the difference between SST anomalies in the western (50° E–70° E,10° N–10° S) and eastern (90° E–110° E, 10° S–0° S) equatorial Indian Ocean during September–November. Both climate indices were standardized to unit variance. Further geographical regions in which the physical and biological variability was investigated in more detail are shown in Figs. 3 and 6 and are as follows: The Eastern Equatorial Indian Ocean (EEIO) region is identical to the eastern box that makes up part of the DMI index; the thermocline ridge region in the southern Indian Ocean (TRIO) is described by 60° E–90° E, 15° S–5° S; the southern Bay of Bengal (SBoB) is described as 85° E–100° E, 0° N–10° N; the southern tip of India (STI) region is described as 70° E–85° E, 2° N–9° N; the western Arabian Sea (WAS) is bounded within 50° E–63° E, 5° N–15° N; and the entire tropical Indian Ocean (TIO) is taken as 40° E–110° E, 25° S–25° N.

In order to extract patterns associated with each mode of variability over the Indian Ocean, we used regression techniques. Since standardized (adimensional) indices were used, the regressions provide values (e.g. $\mathrm{mg\,m^{-3}}$ for SChl) that correspond to the "typical" anomalies associated with IOD and ENSO. Because of the strong correlation between the IOD and ENSO indices (~ 0.53; Yamagata et al., 2004), it is difficult to isolate signals associated with each of those climate modes using regular regression. We therefore employed partial regression techniques to separate the impacts of the two climate modes, as has previously been applied to separate their signals in physical

BGD
10, 5841–5888, 2013

fields (Keerthi et al., 2012). To compute the partial regression between (for example) a time series of chlorophyll anomalies CHL and the IOD index DMI, independently of the ENSO index Niño, one first subtracts signals that are linearly related to ENSO from CHL and DMI, thereafter regressing the residual (denoted "r.") CHL time series on the residual DMI time series, to provide an estimate of CHL variability that is related to IOD, without the effect of ENSO:

$$\mathrm{CHL} = a \cdot \mathrm{Nino} + \mathrm{r.CHL} \quad (1)$$

$$\mathrm{DMI} = b \cdot \mathrm{Nino} + \mathrm{r.DMI} \quad (2)$$

$$\mathrm{r.CHL} = c \cdot \mathrm{r.DMI} + \mathrm{r.r.CHL} \quad (3)$$

The reciprocal partial regression was also performed, removing the IOD signal from ENSO and (in this case) CHL, before regressing their residuals. Proportion of variance explained by partial regressions was estimated as the reduction in residual variance due to the second regression relative to the total original variance:

$$V_{\mathrm{r.DMI}} = \frac{\mathrm{var(r.CHL)} - \mathrm{var(r.r.CHL)}}{\mathrm{var(CHL)}} \quad (4)$$

To complement the partial regression results, partial correlations of anomaly fields to DMI/ENSO indices were additionally calculated as in Yamagata et al. (2004). When interpreting the figures and tables presenting partial regressions and correlations, one has to bear in mind that a proportion of 'joint' variability, which is related to both IOD and ENSO, is removed from the result. Put differently, the explanatory power of 'pure' IOD and 'pure' ENSO signals from partial regressions will frequently add up to less than when they are combined in a multiple regression.

3 SeaWiFS and model comparison

SeaWiFS data and model outputs show overall agreement, though the magnitude and spatial extent of simulated phytoplankton blooms are to some degree overestimated,

BGD
10, 5841–5888, 2013

while intense coastal blooms in SeaWiFS records are lacking in the model. Figure 1 shows the mean seasonal cycle of surface chlorophyll in the model and observations. During the northeast monsoon in boreal winter, elevated SChl concentrations are found over the northwestern part of the Arabian Sea and the northern Bay of Bengal (BoB; Fig. 1a, b). Oligotrophic conditions prevail in the southeastern Arabian Sea, central BoB and in the Southern Hemisphere. These features are relatively well reproduced by the model, although the intensity of the bloom is overestimated along Somalia and around Sri Lanka (Fig. 1b). The spring Inter-monsoon is characterized for both model and observations by oligotrophic conditions and reduced chlorophyll in most of the Indian Ocean basin, likely due to less wind stirring, increased stratification and reduced Ekman pumping (Fig. 1c, d). During the summer/southwest monsoon and fall inter-monsoon (Fig. 1e, h), the model correctly simulates phytoplankton blooms along the coasts of Somalia and the Arabian Peninsula, at the southern tip of India, around Sri Lanka, along the Seychelles Chagos thermocline ridge between 5° S and 15° S and in the southeastern Indian ocean, although the amplitude of these blooms is generally overestimated. Koné et al. (2009) provide a more detailed comparison of the seasonality and the emergent biogeographic provinces that are described from the model and SeaWiFS chlorophyll.

Anomalies during the 1997–1998 ENSO/positive IOD event display similar regional-scale features in SeaWiFS and the model (Fig. 2). The intense positive anomalies along the coastline of Sumatra and Java in fall were well simulated, although their intensity and westward equatorial extension are overestimated by the model (Fig. 2a, b). Weak positive anomalies persist throughout boreal winter in the eastern equatorial Indian Ocean in both SeaWiFS and the model (Fig. 2c, d). The model correctly simulates a chlorophyll bloom in the southeastern Bay of Bengal (north of 4° N and extending to 85° E), which initiated in winter. In addition, the decreased productivity along the western coast and southern tip of India in fall is reasonably well captured by the model, although perhaps slightly overestimated in magnitude. Lastly, the model

BGD
10, 5841–5888, 2013

correctly simulated chlorophyll decreases in the western Arabian Sea in fall and their persistence along the Somalia coast in winter.

Attributing causes to model-data differences is not an easy task since separating forcing errors and physical versus biogeochemical-ecosystem model deficiencies are beyond the scope of this study. The signal to noise ratio of satellite-derived chlorophyll is also an issue that is not addressed here (Ballabrera-Poy et al., 2003) and neither are regionally-specific ecosystem processes such as the dependence on aeolian iron supply (Wiggert and Murtugudde, 2007). In general, broad chlorophyll patterns correspond in the model and SeaWiFS, despite more localized differences, mainly in coastal regions. As a result, we focus our interpretations and discussions of model results below on regional-scale (> 500 km) patterns in the open ocean.

4 Influence of IOD and ENSO in the Indian Ocean

4.1 Physical response

The Indian Ocean presents significant regional contrasts in temporal variability of surface temperature and thermocline depth. Figure 3 shows the standard deviation of deseasoned anomalies of the depth of the 20 °C isotherm (D20; a commonly used proxy of thermocline depth in tropical waters) and sea surface temperature (SST), highlighting the regions of strong interannual variability. Regions of enhanced thermocline depth variations include the Eastern Equatorial Indian Ocean (EEIO), and along the thermocline ridge of the Indian Ocean between 5° S and 10° S (TRIO). These two regions also display enhanced interannual variations of SST due to relatively shallow thermoclines, which result in a strong relationship between SST and thermocline depth (Fig. 3c): vertical movements of the thermocline moderate the amount of mixing, entrainment and upwelling into the surface mixed layer and thereby SST. Three additional regions chosen for further investigation include areas of pronounced thermocline depth variability: The Southern Bay of Bengal (SBoB), Southern Tip of India (STI) and Western Arabian

BGD
10, 5841–5888, 2013

Sea (WAS). The relationship between D20 and SST is insignificant or negative within the first two of these regions, indicating that processes other than vertical mixing and entrainment (such as atmospheric fluxes or lateral advection) influence SST anomalies there.

Mapping the results of partial regression analyses of wind stress, D20 and SST fields reveals dominant spatio-temporal expressions described in the literature (Fig. 4). The physical response to positive IOD events is characterized by a clear zonal gradient of SST and thermocline depth anomalies in the equatorial region (Saji et al., 1999; Webster et al., 1999). Cool SST and a shoaling thermocline develop in boreal summer along the west and south coasts of Sumatra and Java, reaching a peak in intensity during fall (Fig. 4a–d). Positive SST and D20 anomalies occur in the western part of the Indian Ocean in fall, forming a horse-shoe shape that has its strongest expression either side of the equator and persists into winter (Fig. 4c–f). The observed changes in thermocline depth are fueled by surface wind anomalies (Fig. 4, right column): during boreal fall, a strong easterly anomaly arises near the equator, which generates upwelling in the eastern equatorial region, while the associated equatorial Kelvin wave response propagates into the Bay of Bengal and reflects an upwelling Rossby wave offshore (westwards) either side of the equator, as illustrated by the two negative D20 lobes in Fig. 4b and d. Further west, the response is dominated by off-equatorial convergence due to Ekman pumping on the flanks of the equatorial easterly anomaly. The result is a deeper-than-normal D20 in the central and western Indian Ocean, which propagates westwards as symmetrical Rossby wave signals either side of the equator, from fall until the following spring (Fig. 4d, f, h). These deepened thermocline anomalies have a larger amplitude and are more persistent in the Southern Hemisphere, where they interact with the normally-shallow Chagos Seychelles thermocline ridge (Hermes and Reason, 2008; Yokoi et al., 2008). The similarities in spatial patterns of D20 and SST anomalies, together with the regional relationships highlighted in Fig. 3c, suggest that thermocline depth variability is responsible for a large proportion of IOD-linked surface temperature anomalies. Shallow D20 anomalies along the Sumatra-Java coast bring

BGD
10, 5841–5888, 2013

cool water towards the ocean surface (Rao and Behera, 2005); conversely, deep D20 anomalies in the western Indian Ocean isolate surface layers from the influence of cooler waters below, resulting in positive SST anomalies, most evident in fall and winter (Tozuka et al., 2010; Xie et al., 2002). However not all D20 anomalies are mirrored by SST responses. For example, D20 signals in the Bay of Bengal do not cause corresponding signals in overlying SST anomalies, likely due to the insulating effects of the near-surface salinity-stratified barrier layer there (Howden and Murtugudde, 2001; Thadathil et al., 2007).

Our results indicate a less-extensive and weaker ENSO influence on tropical thermocline variations than that of IOD, consistent with studies that attribute Indian Ocean subsurface variability to a dominantly IOD control (e.g. Rao et al., 2002). Figure 5 shows the SST, D20 and wind stress patterns associated with ENSO over the Indian Ocean. Contrasting Figs. 4 and 5 illustrates the distinct surface and subsurface impact of IOD and ENSO in the Indian Ocean (see also Rao and Behera, 2005; Yu et al., 2005). Whereas the IOD-related SST signal dissipates during winter, the basin-wide ENSO signal establishes during winter and peaks in spring (Klein et al., 1999; Xie et al., 2009), about 4–6 months after the mature phase of the IOD. Shallow D20 anomalies develop off the Sumatra coastline and in the eastern Bay of Bengal in response to anomalous equatorial easterlies in winter, while concurrent deepening of the thermocline develops in the southern Indian Ocean in response to Ekman pumping (Fig. 5f). The latter deep anomalies propagate westwards during spring (Fig. 5h), consistent with a Rossby wave signal, but are weaker and centred further south than the corresponding IOD anomalies, congruent with the findings of Rao and Behera (2005) and Yu et al. (2005).

Whereas IOD-related SST effects are largely controlled by wind-driven changes of the thermocline depth as outlined above and in the literature (e.g. Murtugudde et al., 2000; Tozuka et al., 2010; Xie et al., 2002), ENSO-related SST anomalies are mostly a result of changes in surface heat fluxes (such as wind-induced latent heat and solar radiation) caused by anomalous cloud cover and changes in surface winds (Du

BGD
10, 5841–5888, 2013

et al., 2009; Klein et al., 1999), which are in turn driven by adjustments of the ascending and descending branches of the Walker circulation in response to Pacific SST anomalies (Reason et al., 2000; Venzke et al., 2000). As a result there is limited conformity between ENSO-linked SST and D20 anomalies (Fig. 5). Even though ENSO does raise the thermocline near the eastern boundary in winter (Fig. 5f), strong upwelling-favourable winds that might lift these cooler waters to the surface (and thereby transfer the signal to SST) are likely stunted or precluded at this time of year by the monsoon-related wind reversal in the Northern Hemisphere (Schott et al., 2009; Xie et al., 2002).

4.2 Biological response

Certain regions in the Indian Ocean are characterized by pronounced variability in their de-seasoned chlorophyll anomalies (Fig. 6a, b). Within the Arabian Sea, there is enhanced variability of both surface and integrated chlorophyll associated with two known upwelling regions: the Somalia upwelling (within the WAS box) and near the Southern tip of India (STI box). Areas of marked variability of both surface and integrated chlorophyll are also evident in the SBoB and the EEIO. The TRIO area shows marked variability in IChl (Fig. 6a), yet no corresponding signal in SChl (Fig. 6b).

Regression of IChl on D20 reveals a significant negative relationship throughout most of the tropical Indian Ocean (Fig. 6c). Changes in thermocline depth control the proximity of fertile subsurface waters to the sunlit euphotic zone and thereby affect phytoplankton productivity (Lewis et al., 1986; Messié and Chavez, 2012). The downwelling and resultant deep nutricline (thermocline) characteristic of ocean gyres, mean that horizontal advection of nutrients from adjacent regions can play a greater role in chlorophyll responses there than vertical changes in the thermocline depth (McClain et al., 2004), explaining the non-significant coefficients in the gyre regions west of Australia. Similarly, the central Arabian Sea is dominated by Ekman convergence in boreal summer (Schott et al., 2009), which together with strong coastal upwelling and offshore advection of nutrient-rich waters from the Somali coast and western Arabian Sea, might explain the lack of a significant relationship there.

BGD
10, 5841–5888, 2013

SChl anomalies are negatively related to D20 mainly in upwelling regions (Java/Sumatra coast; western coast and southern tip of India; to a lesser degree Somalia and Oman upwelling; Fig. 6d), where shallower thermoclines (nutriclines) would result in entrainment of increased nutrients into surface waters during upwelling. There is however no seasonal upwelling in the central and northern regions of the Arabian Sea and Bay of Bengal; the negative relationship in these areas might be a result of heightened nutrient entrainment by winter mixing events that occur during periods of shallower thermoclines. Wiggert et al. (2002) argue that mixed-layer nutrients are not limiting in the central Arabian Sea and suggest that such a negative relationship might be caused by the thermocline depth regulating a large-amplitude diurnal cycle, the latter of which can cause a greater loss of phytoplankton biomass from the euphotic zone during periods of deep thermoclines than periods of shallower thermoclines. The simulation used here was forced with daily fields however, and so a diurnal effect would not explain the relationship between SChl and D20 anomalies in our case. Beyond those discussed above, most open-ocean regions reveal a weak or insignificant relationship between SChl and D20, indicative that factors beyond the vertical nutricline proximity play a greater role in controlling surface chlorophyll anomalies in these areas.

As expected from the widespread relationship seen in Fig. 6c, IOD-related anomalies of IChl show similar (but opposite) patterns to those of D20 (left panels in Fig. 7 and right panels in Fig. 4, respectively). IOD exerts a striking control on IChl (Fig. 7), predominantly via its substantial influence on regional thermocline depths. The eastern shoaling of D20 results in enhanced productivity along the Java and Sumatra coast and in the southeastern BoB, starting in summer (Fig. 7a) and spreading and intensifying in fall (Fig. 7c). While these anomalies largely dissipate in winter along the Java/Sumatra coast, they persist in the SBoB (Fig. 7e). A horseshoe-shaped pattern of negative chlorophyll anomalies develops in the central and western basin in fall, with strongest expression either side of the equator and greatest persistence in the shallow thermocline ridge region (Fig. 7c, e), similar to the patterns of IOD-related D20 anomalies (Fig. 4d).

BGD
10, 5841–5888, 2013

The SChl signals show spatial patterns that are in many ways similar to those of IChl (Fig. 7a–d): Strong IOD-related positive anomalies develop along the Java and Sumatra coast, starting in boreal summer and peaking in fall, before dissipating in winter. The bloom in the southeastern BoB starts in fall and persists throughout the winter season. The southwestern coast and southern tip of India display a strong chlorophyll decrease in summer and fall. A notable difference between the SChl and IChl anomalies is that the negative western surface anomalies are less extensive and disappear for the most part in winter (Fig. 7f), in contrast to those of IChl, which remain prominent and propagate westwards during this season (Fig. 7e).

As with D20, the biological response to ENSO is generally weaker and occurs later (Fig. 8) compared to that of the IOD (Fig. 7). Positive IChl anomalies develop along the eastern boundary in boreal winter and spring (Fig. 8e, g). Concurrently, lower-than-normal IChl concentrations develop in the TRIO region between $\sim 8^{\circ}$ and 15° S, and also to a lesser degree on the northern side of the equator, with very little expression in SChl (Fig. 8f, h). The largest ENSO-related SChl signal seems to be in fall and winter in the western Arabian Sea, offshore of the Oman and Somalia upwelling region (Fig. 8d, f). A similar, but less extensive signal is seen in IChl anomalies in the same region (Fig. 8c, e, g). ENSO is associated with northeasterly wind anomalies in the western Arabian Sea in boreal fall (Fig. 5d). The Oman and Somalia upwelling systems are likely sensitive to changes in surface winds and these ENSO-related northeasterly anomalies act to reduce upwelling, causing deeper-than-normal thermoclines and warmer-than-normal SSTs (Fig. 5c, d), as well as the chlorophyll impacts noted above.

4.3 Anomalies in key regions

Previously noted differences in the seasonality of ENSO and IOD impacts on Indian Ocean abiotic and biotic variables were more closely examined within specific regions (Fig. 9). In addition to these seasonal differences, there is considerable variability in the

BGD
10, 5841–5888, 2013

impact among different events, as well as apparent asymmetry in their consequences on chlorophyll concentrations in certain regions (Fig. 10).

In the EEIO region, the IOD causes a shoaling of the thermocline, and soon thereafter cool SSTs from June/July to December/January (Fig. 9a). The shallow thermocline promotes entrainment of nutrients and results in anomalously high surface and integrated chlorophyll concentrations from ∼June/July to December (Fig. 9b). Murtugudde et al. (1999) and Wiggert et al. (2009) have previously documented strong phytoplankton blooms in this region during simultaneous positive IOD/El Niño events. Our partial regression analyses attribute those positive anomalies to a dominantly IOD control (Fig. 9b, Tables 1 and 2), with ENSO seemingly exerting a significant influence on the thermocline only from November onwards (Fig. 9a) and causing relatively modest increases of IChl after January (Fig. 9b). Figure 10a shows that the largest positive integrated chlorophyll anomalies in SON correspond to pure IODs, or co-occurring ENSO and IODs, but not pure ENSO events. This, together with the statistics in Tables 1 and 2 and the patterns of partial regression coefficients in Figs. 7 and 8 support our conclusion that anomalous phytoplankton blooms in the EEIO region are predominantly due to IOD forcing. Figure 10a also suggests that positive IChl anomalies in the EEIO region generally tend to be of greater magnitude than negative ones.

In the TRIO region, deeper thermoclines coincide with warmer surface temperatures in response to ENSO and IOD (Fig. 9c), consistent with results of previous studies (Meyers et al., 2007; Rao and Behera, 2005; Xie et al., 2002). The IOD produces slightly earlier thermocline anomalies than ENSO and the ENSO-related surface warming initiates and peaks later than that of IOD. ENSO-related chlorophyll anomalies (both at the surface and over the euphotic layer) seem relatively weak and start to be significant only in boreal winter in this region (Fig. 9d). The clearest biogeochemical signature is seen in response to IOD, with depleted SChl during the IOD peak (∼August to November) and negative IChl coinciding with the deeper-than-normal D20 signal (∼August to April). Although both IOD and ENSO are related to significant negative anomalies during DJF (Table 1), the percentage of chlorophyll variability explained by

BGD
10, 5841–5888, 2013

the IOD is far greater than that of ENSO (Table 2). There is no clear asymmetry between positive and negative chlorophyll anomalies in the TRIO region (Fig. 10b). The largest (negative) anomalies are associated with pure IOD or co-occurring ENSO and IOD events.

In contrast with the two regions discussed above, the SBoB surface temperature and thermocline depth anomalies seem less coupled (Fig. 9e), likely due to a stratified barrier layer isolating the surface temperatures from subsurface influence (Howden and Murtugudde, 2001; Sprintall and Tomczak, 1992; Thadathil et al., 2007; Wiggert et al., 2009). ENSO and IOD both result in shallower-than-normal D20, but only ENSO results in a significant SST change, causing warmer anomalies that start in late fall (Fig. 9e). Similar to other regions, a temporal lag is obvious between IOD and ENSO effects. The prominent shoaling of the thermocline in the central part of the Bay, as a result of an upwelling Rossby wave following a positive IOD event (Fig. 4f), results in an increase in IChl from ~October to February. An increase in SChl in response to the shallower nutricline (shoaling thermocline) occurs only during winter (Fig. 9f), likely because winter cooling and stronger winds allow wind-mixing of the surface layers that are otherwise highly stratified during the remainder of the year (Prasanna Kumar et al., 2010). Positive IChl anomalies are seen in response to ENSO from mid February to early April, although without a significant SChl signal (Fig. 9f), as greater nutrients are brought toward the euphotic zone by a shoaling thermocline, but do not reach surface layers. Although both IOD and ENSO produce significant chlorophyll anomalies (Table 1), IOD variability seems to dominate and explains a far greater proportion of both SChl and IChl anomalies (Table 2). Positive chlorophyll anomalies are generally larger than negative ones in the SBoB region (Fig. 10c) and are never the result of pure ENSO events (but either IOD or IOD + ENSO).

In the STI region, a significant shoaling of D20 develops between ~December and April in response to IOD, preceded by warmer-than-normal SSTs between ~July and January (Fig. 9g). ENSO events also show warming of surface waters, starting in ~November and growing in magnitude until May. During much of the same time

BGD
10, 5841–5888, 2013

(∼ January to May), these warm SST anomalies are accompanied by a shoaling thermocline. The main biogeochemical signal is a decrease of both surface and integrated chlorophyll during IOD events (∼ June/July to December), while ENSO causes a brief period of negative anomalies during winter. During the SON peak expression of climate mode-related anomalies, the IOD signal completely dominates ENSO in terms of explanatory power of the chlorophyll variability (Table 2). The lack of obvious coupling between thermocline depths and surface temperature or chlorophyll in this region is likely due to intense horizontal circulation between the Bay of Bengal and the Arabian Sea (e.g. Vinayachandran et al., 1999), as well as the added complexity of seasonal barrier layers in these regions (Sprintall and Tomczak, 1992). One needs to bear in mind also that meso-scale eddies have been invoked as being important for ecosystem variability in the BoB (Prasanna Kumar et al., 2007), but were not resolved here.

In contrast to all other examined regions, where IOD explains a greater proportion of chlorophyll variability, biological activity in the western Arabian Sea (WAS box in Fig. 6) is predominantly influenced by ENSO (Tables 1 and 2), causing weaker-than-normal SChl and IChl anomalies from ∼ September to the following spring (Fig. 9j). These negative anomalies follow an anomalously deep thermocline between May and November and coincide with warmer-than-normal SST from October onwards (Fig. 9i). The ENSO-linked low-chlorophyll content in this upwelling region may be linked to an anomalously weak monsoon jet in fall (Fig. 5d) and/or early withdrawal of the summer monsoon during ENSO events (Syroka and Toumi, 2004; Xavier et al., 2007). Either way, it is interesting to note that the northeasterly anomalies in SON (Fig. 5d) seem to be preceded by deeper-than-normal D20 starting as early as June. The deeper thermocline likely contributes to lower nutrient concentrations and warmer surface temperatures during upwelling periods, by isolating the cooler nutrient-rich sub-thermocline waters further from the surface. Although these anomalies are significantly related to ENSO, a relatively low proportion (11–15 %) of the de-seasoned chlorophyll variability is explained by the ENSO index (Table 2) and other factors likely play significant roles in driving interannual anomalies in this region. The IOD seems to have relatively little

BGD
10, 5841–5888, 2013

effect in this region, causing a deeper-than-normal thermocline between ~December and April, but neither SST nor chlorophyll anomalies. Figure 10e shows that ENSO or co-occurring IOD/ENSO events generally cause larger chlorophyll anomalies than pure IODs, supporting the statistics in Tables 1 and 2 that point to ENSO but not IOD control of chlorophyll anomalies in the WAS region.

The integrated influences of IOD and ENSO over the entire tropical Indian Ocean basin (TIO) are shown in Fig. 9k and l. At this scale, the IOD has a significant positive effect on D20 from ~September to May, while ENSO seems to display no overall influence on D20 (Fig. 9k). Both climate modes produce warmer-than-average SSTs, with a delayed, longer-lasting and more intense signal for ENSO (~November to May) than for IOD (~October to February; Schott et al., 2009; Xie et al., 2009). Despite the deeper-than-normal D20 associated with IOD, SChl anomalies show a brief positive period during the IOD peak (~August to November), which suggests that the chlorophyll bloom in the eastern pole dominates the basin-wide response during those months. On the other hand, basin-wide IChl becomes significantly less-than-normal in winter and spring in response to IOD (Fig. 9l), driven largely by the horseshoe-shaped negative anomalies in the western basin and thermocline ridge region (Fig. 7e). ENSO-related chlorophyll signals are negative for both surface (~October to February) and depth-integrated values (~January to May), suggestive of an overall negative effect on basin-scale productivity. The positive influence of IOD and negative effect of ENSO on SChl likely counter-act one another during years when these events co-occur, such as in 1997 and 2006.

5 Summary and discussion

The remotely-sensed chlorophyll record is too short to confidently differentiate the relative contributions of IOD and ENSO to interannual variability. As a result, a 41-yr hindcast from a coupled bio-physical general circulation model (NEMO-PISCES) was employed to disentangle anomalies related to IOD and ENSO in the Indian Ocean.

BGD
10, 5841–5888, 2013

Although focus was on the response of chlorophyll, changes in thermocline depth, surface temperature and surface winds were also assessed in order to gain a better understanding of physical processes driving the biological patterns. In comparison with SeaWiFS data, the modelled SChl showed good qualitative agreement of open-ocean seasonal variability and de-seasoned anomalies during the 1997/98 El Niño/positive IOD event. This, despite lacking some of the spatial contrasts or complexity seen in SeaWiFS (especially in coastal regions), which are likely structured by meso- and smaller-scale processes that were not resolved by the simulation. As a result, interpretations were purposefully limited to broad regional patterns.

Although previous studies have not isolated IOD and ENSO signals in chlorophyll anomalies, the patterns described from co-occurring IOD/ENSO events (Murtugudde et al., 1999; Sarma, 2006; Vinayachandran and Mathew, 2003; Wiggert et al., 2009) are consistent with results presented here. Wiggert et al. (2009) use SeaWiFS chlorophyll records to assess the Indian Ocean response to the two positive IOD/El Niño events of 1997 and 2006, and interpret these in light of physical forcing and their resultant impacts on primary productivity. In agreement with our results, they find surface chlorophyll and net primary production increases in the eastern tropical Indian Ocean in boreal fall and in the southeastern Bay of Bengal in winter, as well as negative primary production anomalies in the southwestern Indian Ocean in fall and winter. Although Wiggert et al. (2009) note a negative chlorophyll anomaly around the southern tip of India between October and December in both their two events, the substantial IOD-forced decrease in IChl (and by deduction primary productivity) in this region has not been established elsewhere to the best of our knowledge.

The IOD produces anomalous dynamic (thermocline depth and Rossby-Kelvin wave) and thermodynamic (mixed layer, SST, and heat flux) variability, with phytoplankton communities responding to the sum total of these dynamical-thermodynamical influences on the upper ocean. Across most of the Indian Ocean, IChl changes are strongly related to anomalies of D20 (Fig. 6c), explained by the importance for primary production of the vertical proximity of high-nutrient subsurface waters to the sunlit euphotic

BGD
10, 5841–5888, 2013

layer (Lewis et al., 1986; Messié and Chavez, 2012; Wilson and Adamec, 2002). Messié and Chavez (2012) recently highlighted the dominant role of nutricline depths in controlling changes in chlorophyll and productivity at the global scale. As ENSO and IOD are not orthogonal, their analyses would not effectively separate the signatures of these two modes, and their ENSO-correlated EOFs of chlorophyll and productivity likely contain a proportion of IOD-related expression in the Indian Ocean. Chlorophyll responses to ENSO/IOD are not always symmetrical for positive and negative climate events: negative anomalies tend to be smaller than positive anomalies in some regions (Fig. 10), perhaps because the climatological chlorophyll content is already very low and dominated by regenerated production in those areas.

Our results suggest that ENSO has a weaker and lagged effect on thermocline and chlorophyll anomalies in comparison to IOD. The only region where chlorophyll signals are predominantly related to ENSO (and not IOD) variability, is the western Arabian Sea in (and offshore of) the Oman and Somali upwelling areas. Wiggert et al. (2009) point out a contrasting biological response of the western Arabian Sea to the 1997/98 and 2006/07 events, with an overall decrease of productivity during 1997/98 and a slight increase during 2006/07. Negative chlorophyll and productivity anomalies in this region in 1997/98 have been attributed to IOD (Sarma, 2006), although the co-occurrence of a strong El Niño did not allow the author to distinguish the impacts of the two climate modes. The novel contribution of our study to separate the impacts of ENSO and IOD forcing allows us to suggest that the interannual variability in this region, including that of chlorophyll, is more strongly related to ENSO forcing than to IOD. These findings are supported by Kao and Yu (2009), who show evidence that El Niño events peaking in the eastern Pacific are related to northeasterly wind anomalies and warmer SST in the western Arabian Sea during June–September. Furthermore, Syroka and Toumi (2004) and Xavier et al. (2007) have shown evidence of a shortened summer monsoon linked to El Niño, which would imply a shorter period of active upwelling and likely lower production in those years.

BGD
10, 5841–5888, 2013

Due to opposing regional signals, the basin-scale Indian Ocean phytoplankton response to co-occurring events seems to be weak (Fig. 9; Wiggert et al., 2009). Extensive regional re-organisation does take place however, with significant integrated chlorophyll anomalies occurring over periods of several months in certain regions. As phytoplankton constitute the basal trophic level in pelagic environments, and by their ecology dictate the pathway of energy flow through the ecosystem (Falkowski et al., 1998), such climate-mode anomalies likely have great repercussions for pelagic ecosystems. Disruption of Indian Ocean ecosystems and resources have been attributed to ENSO/IOD events (e.g. Marsac and Le Blanc, 1999; Ménard et al., 2007; Spencer et al., 2000; Vialard et al., 2009), although the necessary biological datasets to detect such disruptions at higher trophic levels are often lacking, especially in the sparsely-sampled tropical pelagic realm. Through the coordinated effort of international research programs such as SIBER (Hood et al., 2010), by increasing the availability of higher resolution and longer-term datasets of physical, biogeochemical and biological variability, and with the use of rapidly progressing coupled ecosystem models to fill in the gaps, we have increasingly exciting and fruitful avenues available to us to develop predictability of climate mode impacts on the physical and biological realms of the Indian Ocean.

Acknowledgements. ML, JV, DK, OA and OM are funded by Institut de Recherche pour le Développement (IRD). ML, OA and OM acknowledge the support of the French ANR, under the grant CEP MACROES (MACRoscope for Oceanic Earth System ANR-09-CEP-003). ML and JV did part of this work as visiting scientists at the National Institute of Oceanography in Goa, India. IRD funding supported JC throughout his Masters degree, from which work this paper was borne, and supported a visit to NIO for him to work on this study with ML and JV. Thanks are due to Raghu Murtugudde for incisive comments that improved the manuscript.

BGD
10, 5841–5888, 2013

References

Abram, N. J., Gagan, M. K., McCulloch, M. T., Chappell, J., and Hantoro, W. S.: Coral reef death during the 1997 Indian Ocean Dipole linked to Indonesian wildfires, Science, 301, 952–955, doi:10.1126/science.1083841, 2003.

Abram, N. J., Gagan, M. G., McCulloch, M. T., Chappell, J., and Hantoro, W. S.: Response to comment on "Coral reef death during the 1997 Indian Ocean Dipole linked to Indonesian wildfires", Science, 303, 1297–1297, doi:10.1126/science.1094047, 2004.

Annamalai, H., Murtugudde, R., Potemra, J., Xie, S. P., Liu, P., and Wang, B.: Coupled dynamics over the Indian Ocean: spring initiation of the Zonal Mode, Deep-Sea Res. Pt. II, 50, 2305–2330, doi:10.1016/S0967-0645(03)00058-4, 2003.

Aumont, O. and Bopp, L.: Globalizing results from ocean in situ iron fertilization studies, Global Biogeochem. Cy., 20, GB2017, doi:10.1029/2005GB002591, 2006.

Aumont, O., Bopp, L., and Schulz, M.: What does temporal variability in aeolian dust deposition contribute to sea-surface iron and chlorophyll distributions?, Geophys. Res. Lett., 35, L07607, doi:10.1029/2007GL031131, 2008.

Ballabrera-Poy, J., Murtugudde, R. G., Christian, J. R., and Busalacchi, A. J.: Signal-to-noise ratios of observed monthly tropical ocean color, Geophys. Res. Lett., 30, 1645, doi:10.1029/2003GL016995, 2003.

Baquero-Bernal, A., Latif, M., and Legutke, S.: On dipolelike variability of sea surface temperature in the tropical Indian Ocean, J. Climate, 15, 1358–1368, doi:10.1175/1520-0442(2002)015<1358:ODVOSS>2.0.CO;2, 2002.

Bjerknes, J.: Atmospheric teleconnections from the equatorial Pacific, Mon. Weather Rev., 97, 163–172, doi:10.1175/1520-0493(1969)097<0163:ATFTEP>2.3.CO;2, 1969.

Blanke, B. and Delecluse, P.: Variability of the tropical Atlantic Ocean simulated by a general circulation model with two different mixed-layer physics, J. Phys. Oceanogr., 23, 1363–1388, doi:10.1175/1520-0485(1993)023<1363:VOTTAO>2.0.CO;2, 1993.

De Boyer Montégut, C., Vialard, J., Shenoi, S. S. C., Shankar, D., Durand, F., Ethé, C., and Madec, G.: Simulated seasonal and interannual variability of the mixed layer heat budget in the northern Indian Ocean, J. Climate, 20, 3249–3268, doi:10.1175/JCLI4148.1, 2007.

Boyer, T., Levitus, S., Garcia, H., Locarnini, R. A., Stephens, C., and Antonov, J.: Objective analyses of annual, seasonal, and monthly temperature and salinity for the World Ocean on a 0.25° grid, Int. J. Climatol., 25, 931–945, doi:10.1002/joc.1173, 2005.

BGD
10, 5841–5888, 2013

Claustre, H., Morel, A., Hooker, S. B., Babin, M., Antoine, D., Oubelkheir, K., Bricaud, A., Leblanc, K., Quéguiner, B., and Maritorena, S.: Is desert dust making oligotrophic waters greener?, Geophys. Res. Lett., 29, 107-1-107-4, doi:10.1029/2001GL014056, 2002.

Cleveland, R. B., Cleveland, W. S., McRae, J. E., and Terpenning, I.: STL: A seasonal-trend decomposition procedure based on loess, Journal of Official Statistics, 6, 3–73, 1990.

Cravatte, S., Madec, G., Izumo, T., Menkes, C., and Bozec, A.: Progress in the 3-D circulation of the eastern equatorial Pacific in a climate ocean model, Ocean Model., 17, 28–48, doi:10.1016/j.ocemod.2006.11.003, 2007.

Dandonneau, Y., Vega, A., Loisel, H., Du Penhoat, Y., and Menkes, C.: Oceanic Rossby Waves acting as a "hay rake" for ecosystem floating by-products, Science, 302, 1548–1551, doi:10.1126/science.1090729, 2003.

Djavidnia, S., Mélin, F., and Hoepffner, N.: Comparison of global ocean colour data records, Ocean Sci., 6, 61–76, doi:10.5194/os-6-61-2010, 2010.

Du, Y., Xie, S.-P., Huang, G., and Hu, K.: Role of air–sea interaction in the long persistence of El Niño–induced north Indian Ocean warming, J. Climate, 22, 2023–2038, doi:10.1175/2008JCLI2590.1, 2009.

Falkowski, P. G., Barber, R. T., and Smetacek, V.: Biogeochemical controls and feedbacks on ocean primary production, Science, 281, 200–206, doi:10.1126/science.281.5374.200, 1998.

Feng, M. and Meyers, G.: Interannual variability in the tropical Indian Ocean: a two-year timescale of Indian Ocean Dipole, Deep-Sea Res. Pt. II, 50, 2263–2284, doi:10.1016/S0967-0645(03)00056-0, 2003.

Geider, R. J., MacIntyre, H. L., and Kana, T. M.: A dynamic regulatory model of phytoplanktonic acclimation to light, nutrients, and temperature, Limnol. Oceanogr., 43, 679–694, 1998.

Goose, H.: Modelling the large-scale behaviour of the coupled ocean–sea-ice system, Ph.D. thesis, Université catholique de Louvain, Belgium, 1997.

Gordon, H. R. and McCluney, W. R.: Estimation of the depth of sunlight penetration in the sea for remote sensing, Appl. Optics, 14, 413–416, 1975.

Hastenrath, S.: Dipoles, temperature gradients, and tropical climate anomalies, B. Am. Meteorol. Soc., 83, 735–738, doi:10.1175/1520-0477(2002)083<0735:WLACNM>2.3.CO;2, 2002.

Hermes, J. C. and Reason, C. J. C.: Annual cycle of the South Indian Ocean (Seychelles-Chagos) thermocline ridge in a regional ocean model, J. Geophys. Res.-Oceans, 113, C04035, doi:10.1029/2007JC004363, 2008.

BGD
10, 5841–5888, 2013

Hood, R. R., Wiggert, J. D., and Naqvi, S. W. A.: A New Basin-wide, International Program in the Indian Ocean, Ocean Carbon and Biogeochemistry News, 3, 5–8, 2010.
Horii, T., Hase, H., Ueki, I., and Masumoto, Y.: Oceanic precondition and evolution of the 2006 Indian Ocean dipole, Geophys. Res. Lett., 35, L03607, doi:10.1029/2007GL032464, 2008.
Howden, S. D. and Murtugudde, R.: Effects of river inputs into the Bay of Bengal, J. Geophys. Res.-Oceans, 106, 19825–19843, doi:10.1029/2000JC000656, 2001.
Iskandar, I., Rao, S., and Tozuka, T.: Chlorophyll *a* bloom along the southern coasts of Java and Sumatra during 2006, Int. J. Remote Sens., 30, 663–671, 2009.
Izumo, T., Vialard, J., Lengaigne, M., De Boy, C., Behera, S. K., Luo, J.-J., Cravatte, S., Masson, S., and Yamagata, T.: Influence of the state of the Indian Ocean Dipole on the following year's El Niño, Nat. Geosci., 3, 168–172, doi:10.1038/ngeo760, 2010.
Jackett, D. R. and Mcdougall, T. J.: Minimal adjustment of hydrographic profiles to achieve static stability, J. Atmos. Ocean. Tech., 12, 381–389, doi:10.1175/1520-0426(1995)012<0381:MAOHPT>2.0.CO;2, 1995.
Kao, H.-Y. and Yu, J.-Y.: Contrasting eastern-Pacific and central-Pacific types of ENSO, J. Climate, 22, 615–632, doi:10.1175/2008JCLI2309.1, 2009.
Keerthi, M., Lengaigne, M., Vialard, J., De Boyer Montégut, C., and Muraleedharan, P.: Interannual variability of the Tropical Indian Ocean mixed layer depth, Clim. Dynam., 38, 1–17, doi:10.1007/s00382-012-1295-2, 2012.
Klein, S. A., Soden, B. J., and Lau, N. C.: Remote sea surface temperature variations during ENSO: Evidence for a tropical atmospheric bridge, J. Climate, 12, 917–932, doi:10.1175/1520-0442(1999)012<0917:RSSTVD>2.0.CO;2, 1999.
Koné, V., Aumont, O., Levy, C., and Resplandy, L.: Physical and biogeochemical controls of the phytoplankton seasonal cycle in the Indian Ocean: a modeling study, in: Indian Ocean Biogeochemical Processes and Ecological Variability, vol. 185, edited by: Wiggert, J. D., Hood, R. R., Wajih, S., Naqvi, A., Brink, K. H., and Smith, S. L., 350 pp., 2009.
Lengaigne, M. and Vecchi, G.: Contrasting the termination of moderate and extreme El Niño events in coupled general circulation models, Clim. Dynam., 35, 299–313, doi:10.1007/s00382-009-0562-3, 2010.
Lengaigne, M., Boulanger, J.-P., Menkes, C., Masson, S., Madec, G., and Delecluse, P.: Ocean response to the March 1997 Westerly Wind Event, J. Geophys. Res.-Oceans, 107, 8015, doi:10.1029/2001JC000841, 2002.

BGD
10, 5841–5888, 2013

Lengaigne, M., Madec, G., Menkes, C., and Alory, G.: Impact of isopycnal mixing on the tropical ocean circulation, J. Geophys. Res.-Oceans, 108, 3345, doi:10.1029/2002JC001704, 2003.
Lengaigne, M., Boulanger, J.-P., Menkes, C., and Spencer, H.: Influence of the seasonal cycle on the termination of El Niño events in a coupled general circulation model, J. Climate, 19, 1850–1868, doi:10.1175/JCLI3706.1, 2006.
Lengaigne, M., Menkes, C., Aumont, O., Gorgues, T., Bopp, L., André, J.-M., and Madec, G.: Influence of the oceanic biology on the tropical Pacific climate in a coupled general circulation model, Clim. Dynam., 28, 503–516, doi:10.1007/s00382-006-0200-2, 2007.
Lengaigne, M., Hausmann, U., Madec, G., Menkes, C., Vialard, J., and Molines, J.: Mechanisms controlling warm water volume interannual variations in the equatorial Pacific: diabatic versus adiabatic processes, Clim. Dynam., 38, 1031–1046, doi:10.1007/s00382-011-1051-z, 2012.
Lewis, M. R., Hebert, D., Harrison, W., Platt, T., and Oakey, N. S.: Vertical nitrate fluxes in the oligotrophic ocean, Science, 234, 870, 1986.
Madec, G., Delecluse, P., Imbard, M., and Lévy, C.: OPA 8.1 Ocean General Circulation Model Reference Manual, Note du Pôle de Modélisation, IPSL, Paris, 1998.
Maritorena, S., D' Andon, O. H. F., Mangin, A., and Siegel, D. A.: Merged satellite ocean color data products using a bio-optical model: characteristics, benefits and issues, Remote Sens. Environ., 114, 1791–1804, doi:10.1016/j.rse.2010.04.002, 2010.
Marsac, F. and Le Blanc, J. L.: Oceanographic changes during the 1997-1998 El Niño in the Indian Ocean and their impact on the purse seine fishery, IOTC Proceedings, 2, 147–157, 1999.
Maury, O.: An overview of APECOSM, a spatialized mass balanced "Apex Predators ECOSystem Model" to study physiologically structured tuna population dynamics in their ecosystem, Prog. Oceanogr., 84, 113–117, doi:10.1016/j.pocean.2009.09.013, 2010.
McClain, C. R., Signorini, S. R., and Christian, J. R.: Subtropical gyre variability observed by ocean-color satellites, Deep-Sea Res. Pt. II, 51, 281–301, doi:10.1016/j.dsr2.2003.08.002, 2004.
McPhaden, M. J., Zebiak, S. E., and Glantz, M. H.: ENSO as an Integrating Concept in Earth Science, Science, 314, 1740–1745, doi:10.1126/science.1132588, 2006.
Ménard, F., Marsac, F., Bellier, E., and Cazelles, B.: Climatic oscillations and tuna catch rates in the Indian Ocean: a wavelet approach to time series analysis, Fish. Oceanogr., 16, 95–104, doi:10.1111/j.1365-2419.2006.00415.x, 2007.

BGD
10, 5841–5888, 2013

Messié, M. and Chavez, F. P.: A global analysis of ENSO synchrony: The oceans' biological response to physical forcing, J. Geophys. Res.-Oceans, 117, C09001, doi:10.1029/2012JC007938, 2012.
Meyers, G., McIntosh, P., Pigot, L., and Pook, M.: The years of El Niño, La Niña, and interactions with the tropical Indian Ocean, J. Climate, 20, 2872–2880, doi:10.1175/JCLI4152.1, 2007.
Morel, A. and Maritorena, S.: Bio-optical properties of oceanic waters: a reappraisal, J. Geophys. Res.-Oceans, 106, 7163–7180, doi:10.1029/2000JC000319, 2001.
Morel, A., Huot, Y., Gentili, B., Werdell, P. J., Hooker, S. B., and Franz, B. A.: Examining the consistency of products derived from various ocean color sensors in open ocean (Case 1) waters in the perspective of a multi-sensor approach, Remote Sens. Environ., 111, 69–88, doi:10.1016/j.rse.2007.03.012, 2007.
Murtugudde, R. and Busalacchi, A. J.: Interannual variability of the dynamics and thermodynamics of the tropical Indian Ocean, J. Climate, 12, 2300–2326, doi:10.1175/1520-0442(1999)012<2300:IVOTDA>2.0.CO;2, 1999.
Murtugudde, R. G., Signorini, S. R., Christian, J. R., Busalacchi, A. J., McClain, C. R., and Picaut, J.: Ocean color variability of the tropical Indo-Pacific basin observed by SeaWiFS during 1997–1998, J. Geophys. Res.-Oceans, 104, 18351–18366, 1999.
Murtugudde, R. G., McCreary, J. P., and Busalacchi, A. J.: Oceanic processes associated with anomalous events in the Indian Ocean with relevance to 1997–1998, J. Geophys. Res.-Oceans, 105, 3295–3306, doi:10.1029/1999JC900294, 2000.
Murtugudde, R., Wang, L., Hackert, E., Beauchamp, J., Christian, J., and Busalacchi, A. J.: Remote sensing of the Indo-Pacific region: ocean colour, sea level, winds and sea surface temperatures, Int. J. Remote Sens., 25, 1423–1435, doi:10.1080/01431160310001592391, 2004.
Nidheesh, A. G., Lengaigne, M., Vialard, J., Unnikrishnan, A. S., and Dayan, H.: Decadal and long-term sea level variability in the tropical Indo-Pacific Ocean, Clim. Dynam., in press, doi:10.1007/s00382-012-1463-4, 2012.
O'Reilly, J. E., Maritorena, S., Mitchell, B. G., Siegel, D. A., Carder, K. L., Garver, S. A., Kahru, M., and McClain, C.: Ocean color chlorophyll algorithms for SeaWiFS, J. Geophys. Res.-Oceans, 103, 24937–24953, 1998.
Paulson, C. A. and Simpson, J. J.: Irradiance measurements in the upper ocean, J. Phys. Oceanogr., 7, 952–956, 1977.

BGD
10, 5841–5888, 2013

Prasanna Kumar, S., Nuncio, M., Ramaiah, N., Sardesai, S., Narvekar, J., Fernandes, V., and Paul, J. T.: Eddy-mediated biological productivity in the Bay of Bengal during fall and spring intermonsoons, Deep-Sea Res. Pt. I, 54, 1619–1640, doi:10.1016/j.dsr.2007.06.002, 2007.

Prasanna Kumar, S., Nuncio, M., Narvekar, J., Ramaiah, N., Sardessai, S., Gauns, M., Fernandes, V., Paul, J. T., Jyothibabu, R., and Jayaraj, K. A.: Seasonal cycle of physical forcing and biological response in the Bay of Bengal, Indian J. Mar. Sci., 39, 388–405, 2010.

Rao, S. A. and Behera, S. K.: Subsurface influence on SST in the tropical Indian Ocean: structure and interannual variability, Dynam. Atmos. Oceans, 39, 103–135, doi:10.1016/j.dynatmoce.2004.10.014, 2005.

Rao, S. A., Behera, S. K., Masumoto, Y., and Yamagata, T.: Interannual subsurface variability in the tropical Indian Ocean with a special emphasis on the Indian Ocean Dipole, Deep-Sea Res. Pt. II, 49, 1549–1572, doi:10.1016/S0967-0645(01)00158-8, 2002.

R Development Core Team: R: A language and environment for statistical computing, Vienna, Austria. Available at: http://www.R-project.org, 2011.

Reason, C. J. C., Allan, R. J., Lindesay, J. A., and Ansell, T. J.: ENSO and climatic signals across the Indian Ocean Basin in the global context: Part I, interannual composite patterns, Int. J. Climatol., 20, 1285–1327, doi:10.1002/1097-0088(200009)20:11<1285::AID-JOC536>3.0.CO;2-R, 2000.

Reverdin, G., Cadet, D. L., and Gutzler, D.: Interannual displacements of convection and surface circulation over the equatorial Indian Ocean, Q. J. Roy. Meteor. Soc., 112, 43–67, doi:10.1002/qj.49711247104, 1986.

Rodgers, K. B., Aumont, O., Menkes, C., and Gorgues, T.: Decadal variations in equatorial Pacific ecosystems and ferrocline/pycnocline decoupling, Global Biogeochem. Cy., 22, GB2019, doi:10.1029/2006GB002919, 2008.

Saji, N. H., Goswami, B. N., Vinayachandran, P. N., and Yamagata, T.: A dipole mode in the tropical Indian Ocean, Nature, 401, 360–363, 1999.

Sarma, V. V. S. S.: The influence of Indian Ocean Dipole (IOD) on biogeochemistry of carbon in the Arabian Sea during 1997–1998, J. Earth Syst. Sci., 115, 433–450, doi:10.1007/BF02702872, 2006.

Schott, F. A., Xie, S.-P., and McCreary, J. P.: Indian Ocean circulation and climate variability, Rev. Geophys., 47, RG1002, doi:10.1029/2007RG000245, 2009.

Song, Q., Vecchi, G. A., and Rosati, A. J.: Indian Ocean variability in the GFDL coupled climate model, J. Climate, 20, 2895–2916, doi:10.1175/JCLI4159.1, 2007.

BGD
10, 5841–5888, 2013

Song, Q., Vecchi, G. A., and Rosati, A. J.: Predictability of the Indian Ocean sea surface temperature anomalies in the GFDL coupled model, Geophys. Res. Lett., 35, L02701, doi:10.1029/2007GL031966, 2008.
Spencer, T., Teleki, K. A., Bradshaw, C., and Spalding, M. D.: Coral Bleaching in the Southern Seychelles During the 1997–1998 Indian Ocean Warm Event, Mar. Pollut. Bull., 40, 569–586, doi:10.1016/S0025-326X(00)00026-6, 2000.
Sprintall, J. and Tomczak, M.: Evidence of the barrier layer in the surface layer of the tropics, J. Geophys. Res.-Oceans, 97, 7305–7316, doi:10.1029/92JC00407, 1992.
Susanto, R. D. and Marra, J.: Effects of the 1997/98 El Niño on chlorophyll *a* variability along the southern coasts of Java and Sumatra, Oceanography, 18, 124–127, 2005.
Syroka, J. and Toumi, R.: On the withdrawal of the Indian summer monsoon, Q. J. Roy. Meteor. Soc., 130, 989–1008, doi:10.1256/qj.03.36, 2004.
Takahashi, T., Broecker, W. S., and Langer, S.: Redfield ratio based on chemical data from isopycnal surfaces, J. Geophys. Res.-Oceans, 90, 6907–6924, doi:10.1029/JC090iC04p06907, 1985.
Thadathil, P., Muraleedharan, P. M., Rao, R. R., Somayajulu, Y. K., Reddy, G. V., and Revichandran, C.: Observed seasonal variability of barrier layer in the Bay of Bengal, J. Geophys. Res.-Oceans, 112, doi:10.1029/2006JC003651, 2007.
Timmermann, R., Goosse, H., Madec, G., Fichefet, T., Ethe, C., and Dulière, V.: On the representation of high latitude processes in the ORCA-LIM global coupled sea ice–ocean model, Ocean Model., 8, 175–201, C02009, doi:10.1016/j.ocemod.2003.12.009, 2005.
Tozuka, T., Yokoi, T., and Yamagata, T.: A modeling study of interannual variations of the Seychelles Dome, J. Geophys. Res.-Oceans, 115, 04005, doi:10.1029/2009JC005547, 2010.
Trenberth, K. E.: The definition of El Niño, B. Am. Meteorol. Soc., 78, 2771–2777, 1997.
Trenberth, K. E., Olson, J. G., and Large, W. G.: A global ocean wind stress climatology based on ECMWF analyses, Climate and Global Dynamics Division, National Center for Atmospheric Research, Boulder, Colorado, 1989.
Uppala, S. M., KÅllberg, P. W., Simmons, A. J., Andrae, U., Bechtold, V. D. C., Fiorino, M., Gibson, J. K., Haseler, J., Hernandez, A., Kelly, G. A., Li, X., Onogi, K., Saarinen, S., Sokka, N., Allan, R., Andersson, E., Arpe, K., Balmaseda, M., Beljaars, A., van de Berg, L., Bidlot, J., Bormann, N., Caires, S., Chevallier, F., Dethof, A., Dragosavac, M., Fisher, M., Fuentes, M., Hagemann, S., Holm, E., Hoskins, B., Isaksen, L., Janssen, P., Jenne, R., McNally, A., Mahfouf, J.-F., Morcrette, J.-J., Rayner, N., Saunders, R., Simon, P., Sterl, A., Trenberth, K.,

BGD
10, 5841–5888, 2013

Untch, A., Vasiljevic, D., Viterbo, P., and Woollen, J.: The ERA-40 re-analysis, Q. J. Roy. Meteor. Soc., 131, 2961–3012, 2005.
Venzke, S., Latif, M., and Villwock, A.: Coupled GCM ECHO-2, Part II: Indian ocean response to ENSO, J. Climate, 13, 1371–1383, 2000.
Vialard, J., Duvel, J. P., Mcphaden, M. J., Bouruet-Aubertot, P., Ward, B., Key, E., Bourras, D., Weller, R., Minnett, P., Weill, A., Cassou, C., Eymard, L., Fristedt, T., Basdevant, C., Dandonneau, Y., Duteil, O., Izumo, T., de Boyer Montégut, C., Masson, S., Marsac, F., Menkes, C., and Kennan, S.: Cirene: Air-Sea Interactions in the Seychelles-Chagos Thermocline Ridge Region, B. Am. Meteorol. Soc., 90, 45–61, 2009.
Vinayachandran, P. N. and Mathew, S.: Phytoplankton bloom in the Bay of Bengal during the northeast monsoon and its intensification by cyclones, Geophys. Res. Lett., 30, 1572, doi:10.1029/2002GL016717, 2003.
Vinayachandran, P. N., Masumoto, Y., Mikawa, T., and Yamagata, T.: Intrusion of the Southwest Monsoon Current into the Bay of Bengal, J. Geophys. Res.-Oceans, 104, 11077–11, 085, doi:10.1029/1999JC900035, 1999.
Vinayachandran, P. N., Iizuka, S., and Yamagata, T.: Indian Ocean dipole mode events in an ocean general circulation model, Deep-Sea Res. Pt. II, 49, 1573–1596, doi:10.1016/S0967-0645(01)00157-6, 2002.
Vinueza, L. R., Branch, G. M., Branch, M. L., and Bustamante, R. H.: Top-down herbivory and bottom-up El Niño effects on Galápagos rocky-shore communities, Ecol. Monogr., 76, 111–131, doi:10.1890/04-1957, 2006.
Wang, C. and Fiedler, P. C.: ENSO variability and the eastern tropical Pacific: a review, Prog. Oceanogr., 69, 239–266, doi:10.1016/j.pocean.2006.03.004, 2006.
Webster, P. J., Moore, A. M., Loschnigg, J. P., and Leben, R. R.: Coupled ocean-atmosphere dynamics in the Indian Ocean during 1997–1998, Nature, 401, 356–60, doi:10.1038/43848, 1999.
Wiggert, J. D. and Murtugudde, R. G.: The sensitivity of the southwest monsoon phytoplankton bloom to variations in aeolian iron deposition over the Arabian Sea, J. Geophys. Res.-Oceans, 112, C05005, doi:10.1029/2006JC003514, 2007.
Wiggert, J., Murtugudde, R., and McClain, C.: Processes controlling interannual variations in wintertime (Northeast Monsoon) primary productivity in the central Arabian Sea, Deep-Sea Res. Pt. II, 49, 2319–2343, doi:10.1016/S0967-0645(02)00039-5, 2002.

BGD
10, 5841–5888, 2013

Wiggert, J. D., Hood, R. R., Banse, K., and Kindle, J. C.: Monsoon-driven biogeochemical processes in the Arabian Sea, Prog. Oceanogr., 65, 176–213, doi:10.1016/j.pocean.2005.03.008, 2005.

Wiggert, J. D., Murtugudde, R. G., and Christian, J. R.: Annual ecosystem variability in the tropical Indian Ocean: results of a coupled bio-physical ocean general circulation model, Deep-Sea Res. Pt. II, 53, 644–676, doi:10.1016/j.dsr2.2006.01.027, 2006.

Wiggert, J. D., Vialard, J., and Behrenfeld, M. J.: Basinwide modification of dynamical and biogeochemical processes by the positive phase of the Indian Ocean Dipole during the Sea-WiFS era, in: Indian Ocean Biogeochemical Processes and Ecological Variability, vol. 185, edited by: Wiggert, J. D., Hood, R. R., Wajih, S., Naqvi, A., Brink, K. H., and Smith, S. L., 350.pp., 2009.

Wilson, C. and Adamec, D.: A global view of bio-physical coupling from SeaWiFS and TOPEX satellite data, 1997–2001, Geophys. Res. Lett., 29, 1257, doi:10.1029/2001GL014063, 2002.

Van Woesik, R.: Comment on "Coral reef death during the 1997 Indian Ocean Dipole linked to Indonesian wildfires", Science, 303, 1297–1297, doi:10.1126/science.1091983, 2004.

Xavier, P. K., Marzin, C., and Goswami, B. N.: An objective definition of the Indian summer monsoon season and a new perspective on the ENSO–monsoon relationship, Q. J. Roy. Meteor. Soc., 133, 749–764, doi:10.1002/qj.45, 2007.

Xie, P. and Arkin, P. A.: Global precipitation: A 17-yr monthly analysis based on gauge observations, satellite estimates, and numerical model outputs, B. Am. Meteorol. Soc., 78, 2539–2558, 1997.

Xie, S.-P., Annamalai, H., Schott, F. A., and McCreary, J. P.: Structure and mechanisms of south Indian Ocean climate variability, J. Climate, 15, 864–878, doi:10.1175/1520-0442(2002)015<0864:SAMOSI>2.0.CO;2, 2002.

Xie, S. P., Hafner, J., Tokinaga, H., Du, Y., Sampe, T., and Hu KaiMing, H. G.: Indian Ocean capacitor effect on Indo-western Pacific climate during the summer following El Niño, J. Climate, 22, 730–747, doi:10.1175/2008JCLI2544.1, 2009.

Yamagata, T., Behera, S. K., Luo, J. J., Masson, S., Jury, M. R., and Rao, S. A.: Coupled ocean-atmosphere variability in the tropical Indian Ocean, Geoph. Monog. Series, 147, 189–211, doi:10.1029/147GM12., 2004.

BGD
10, 5841–5888, 2013

Yoder, J. A. and Kennelly, M. A.: Seasonal and ENSO variability in global ocean phytoplankton chlorophyll derived from 4 yr of SeaWiFS measurements, Global Biogeochem. Cy., 17, 1112, doi:10.1029/2002GB001942, 2003.

Yokoi, T., Tozuka, T., and Yamagata, T.: Seasonal Variation of the Seychelles Dome, J. Climate, 21, 3740–3754, doi:10.1175/2008JCLI1957.1, 2008.

Yu, W., Xiang, B., Liu, L., and Liu, N.: Understanding the origins of interannual thermocline variations in the tropical Indian Ocean, Geophys. Res. Lett., 32, 24706, doi:10.1029/2005GL024327, 2005.

Zhang, Y., Rossow, W. B., Lacis, A. A., Oinas, V., and Mishchenko, M. I.: Calculation of radiative fluxes from the surface to top of atmosphere based on ISCCP and other global data sets: Refinements of the radiative transfer model and the input data, J. Geophys. Res.-Atmos., 109, 19105, doi:10.1029/2003JD004457, 2004.

BGD
10, 5841–5888, 2013

Table 1. Partial regression coefficients (and partial correlation coefficients in brackets) of IChl ($mg\,m^{-2}$) and SChl ($mg\,m^{-3}$) signals versus the relevant climate index (DMI and Niño3.4). The season shown is that in which the multiple regression including IOD+ENSO explains the greatest proportion of chlorophyll variance, which is quoted in Table 2. Bold figures denote significant regression or correlation coefficients ($p < 0.05$).

		IChl			SChl	
Region	Season	IOD	ENSO	Season	IOD	ENSO
EEIO	SON	**3.015 (0.92)**	−0.237 (−0.18)	SON	**0.180 (0.94)**	−0.012 (−0.19)
TRIO	DJF	**−0.873 (−0.74)**	**−0.411 (−0.46)**	SON	**−0.015 (−0.50)**	0.003 (0.14)
SBoB	DJF	**1.272 (0.67)**	0.510 (0.29)	DJF	**0.044 (0.57)**	0.013 (0.20)
STI	SON	**−1.404 (−0.72)**	0.113 (0.08)	SON	**−0.062 (−0.62)**	−0.006 (−0.07)
WAS	MAM	0.207 (0.18)	**−0.461 (−0.38)**	DJF	0.007 (0.12)	**−0.020 (−0.34)**
TIO	DJF	**−0.162 (−0.54)**	**−0.090 (−0.34)**	SON	**0.011 (0.44)**	**−0.007 (−0.32)**

BGD
10, 5841–5888, 2013

Table 2. Percentage of interannual variance (within the indicated season) of IChl and SChl explained by regressions including IOD+ENSO as explanatory variables (first column) and for the partial regression of each climate mode in isolation (2nd and 3rd columns). Bold figures indicate when partial regressions resulted in a significant coefficient ($p < 0.05$).

		IChl				SChl		
Region	Season	IOD+ENSO	IOD	ENSO	Season	IOD+ENSO	IOD	ENSO
EEIO	SON	89	**62**	0	SON	92	**64**	0
TRIO	DJF	77	**27**	**6**	SON	28	**24**	2
SBoB	DJF	68	**26**	4	DJF	52	**23**	2
STI	SON	60	**42**	0	SON	53	**30**	0
WAS	MAM	15	3	**15**	DJF	12	4	**11**
TIO	DJF	56	**18**	**6**	SON	20	**20**	**9**

BGD
10, 5841–5888, 2013

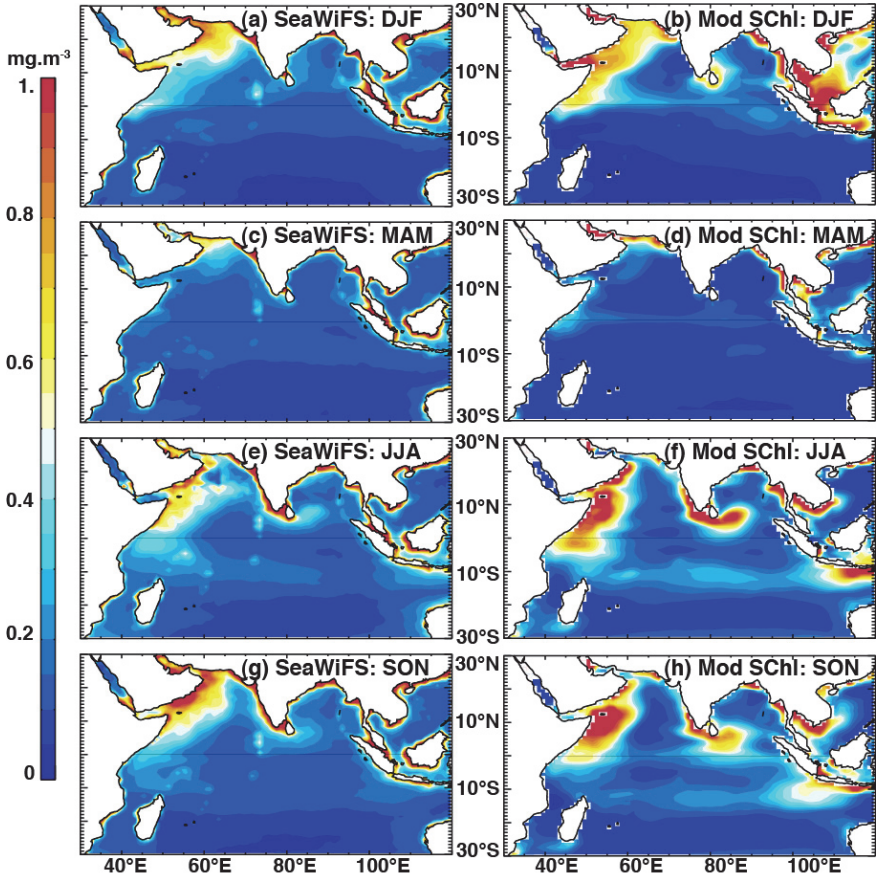

Fig. 1. Seasonal evolution of average SChl patterns from SeaWiFS satellite estimates (left panels) and model outputs (right panels). Seasons are represented as December–February (DJF), March–May (MAM), June–August (JJA) and September–November (SON). The seasonal cycle is calculated over the 1998–2009 period for observations and 1990–2001 for the model.

BGD
10, 5841–5888, 2013

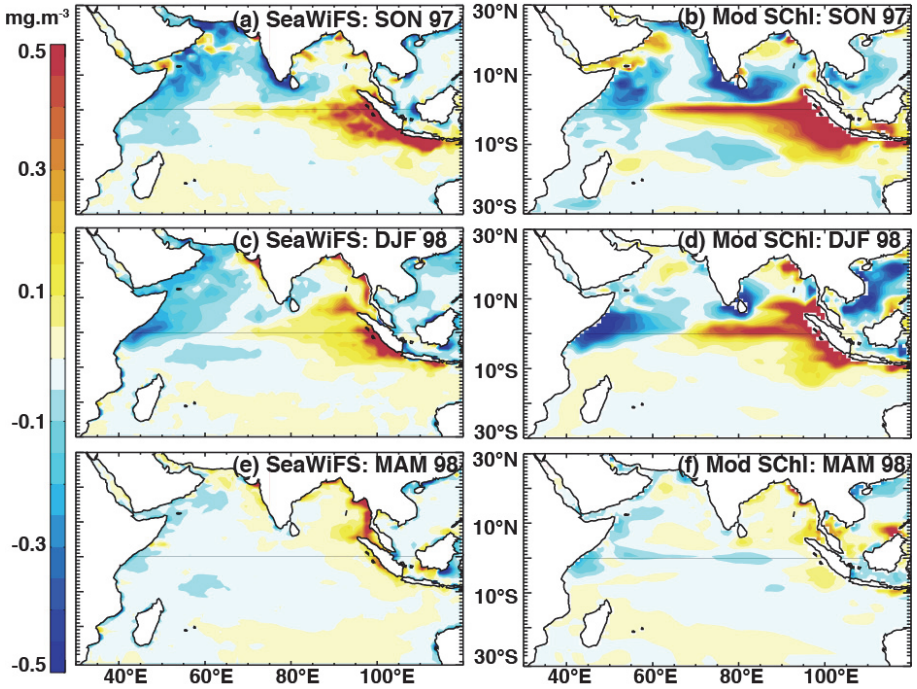

Fig. 2. De-seasoned anomalies of SChl patterns during the 1997/1998 event from SeaWiFS satellite estimates (left panels) and model outputs (right panels). Anomalies are calculated with respect to a 1998–2009 climatology for SeaWiFS and a 1990–2001 climatology for the model. Season abbreviations as in Fig. 1.

BGD
10, 5841–5888, 2013

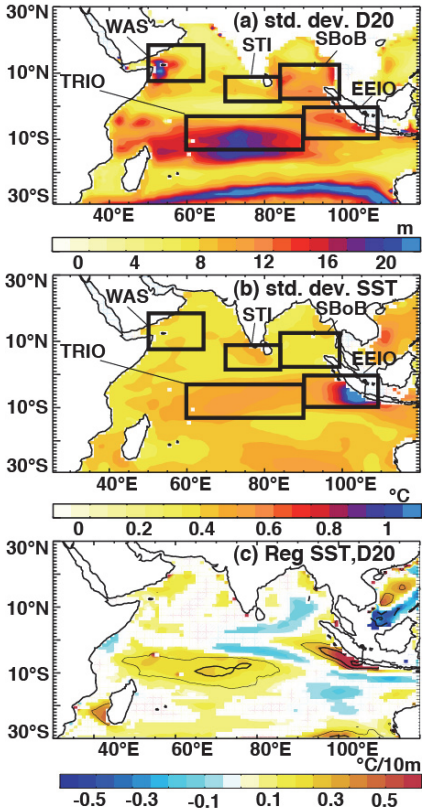

Fig. 3. Standard deviation of de-seasoned anomalies of **(a)** D20 and **(b)** SST over the period of 1961–2001. **(c)** Coefficients of SST anomalies regressed onto D20 anomalies from the same period. Signals are shown when above a 90 % significance level. Thin, normal and thick contours indicate correlation coefficients of 0.4, 0.6 and 0.8, respectively. Plain (dashed) lines represent positive (negative) coefficients. Geographical boxes used in later analyses are shown on panels **(a)** and **(b)**.

BGD
10, 5841–5888, 2013

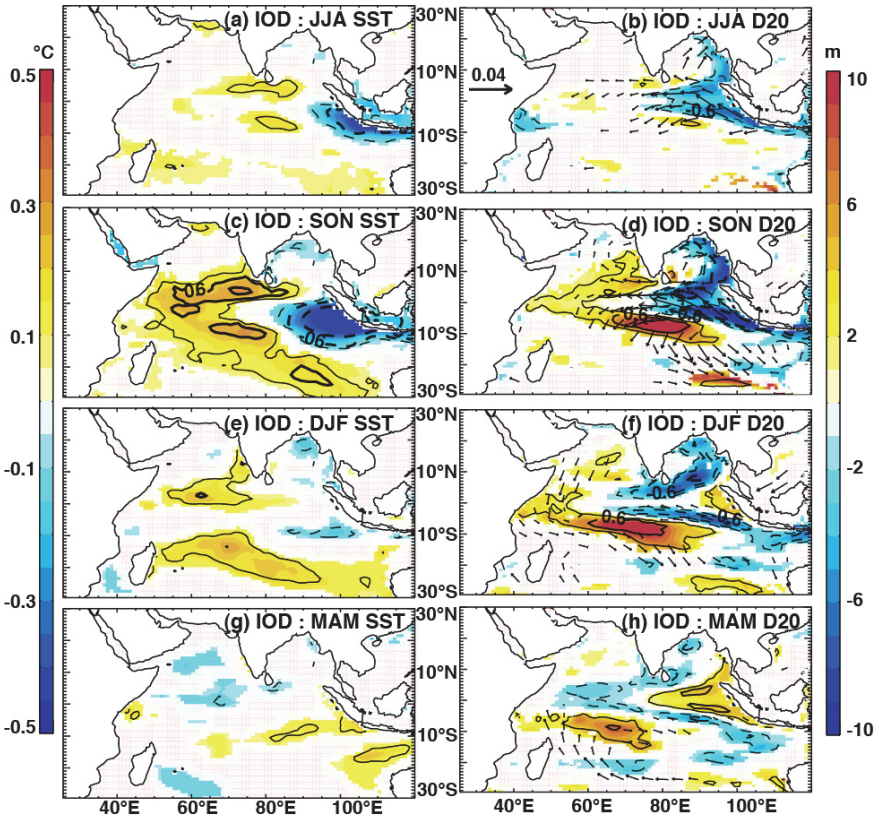

Fig. 4. Partial regression coefficients of de-seasoned anomalies of SST (left panels), D20 (colour; right panels) and wind stress (arrows; right panels) as regressed onto the IOD index, with the influence of ENSO removed. Regression coefficients are computed for the 1961–2001 period and are shown when beyond a 90 % significance level. Thin, normal and thick contours indicate correlation coefficients of 0.4, 0.6 and 0.8, respectively. Plain (dashed) lines represent positive (negative) correlations.

BGD
10, 5841–5888, 2013

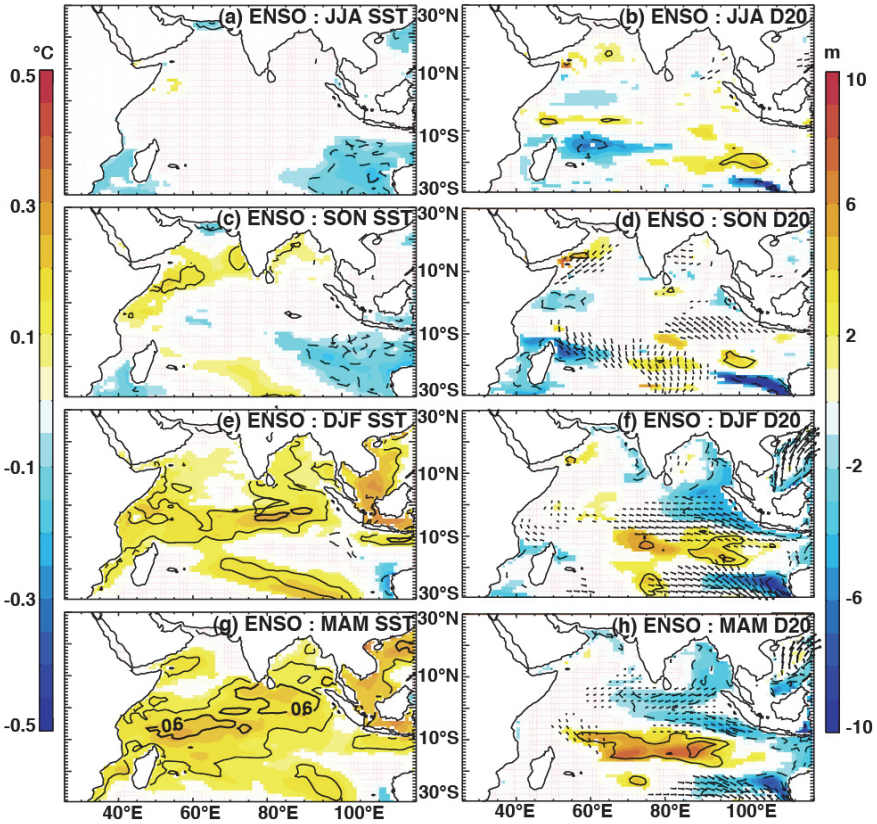

Fig. 5. Partial regression coefficients of de-seasoned anomalies of SST (left panels), D20 (colour; right panels) and wind stress (arrows; right panels) as regressed onto the ENSO index, with the influence of IOD removed. Regression coefficients are computed for the 1961–2001 period and are shown when beyond a 90 % significance level. Thin, normal and thick contours indicate correlation coefficients of 0.4, 0.6 and 0.8, respectively. Plain (dashed) lines represent positive (negative) correlations.

BGD
10, 5841–5888, 2013

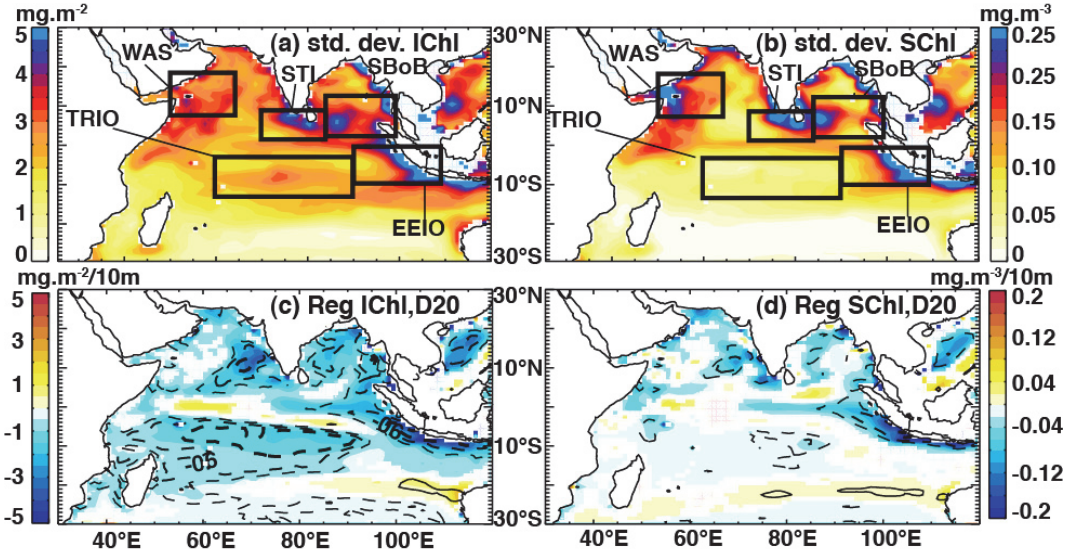

Fig. 6. Standard deviation of de-seasoned anomalies of **(a)** IChl and **(b)** SChl over the period of 1961–2001. **(c)** Coefficients of IChl and **(d)** SChl anomalies regressed onto D20 anomalies from the same period. Signals are shown when beyond a 90 % significance level. Thin, normal and thick contours indicate correlation coefficients of 0.4, 0.6 and 0.8, respectively. Plain (dashed) lines represent positive (negative) coefficients. Geographical boxes used in later analyses and selected on the basis of regional biogeochemical variability are shown on panels **(a)** and **(b)**.

BGD
10, 5841–5888, 2013

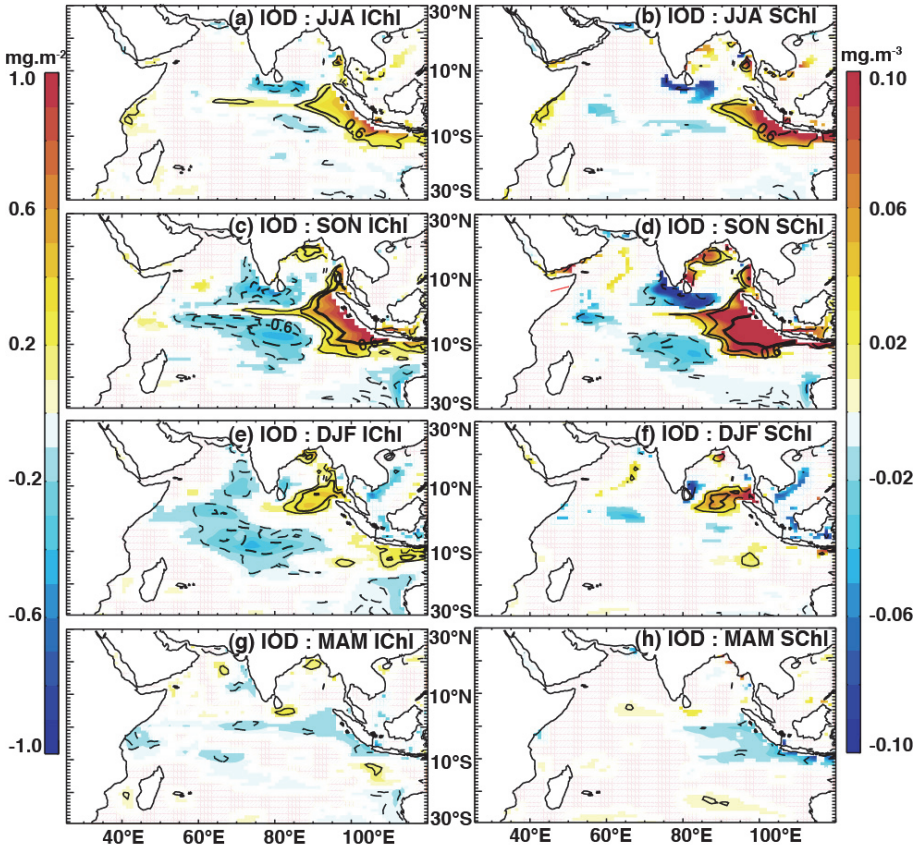

Fig. 7. Partial regression coefficients of de-seasoned anomalies of IChl (left panels) and SChl (right panels) as regressed onto the IOD index, with the influence of ENSO removed. Regression coefficients are computed for the 1961–2001 period and are shown when beyond a 90 % significance level. Thin, normal and thick contours indicate correlation coefficients of 0.4, 0.6 and 0.8, respectively. Plain (dashed) lines represent positive (negative) correlations.

BGD
10, 5841–5888, 2013

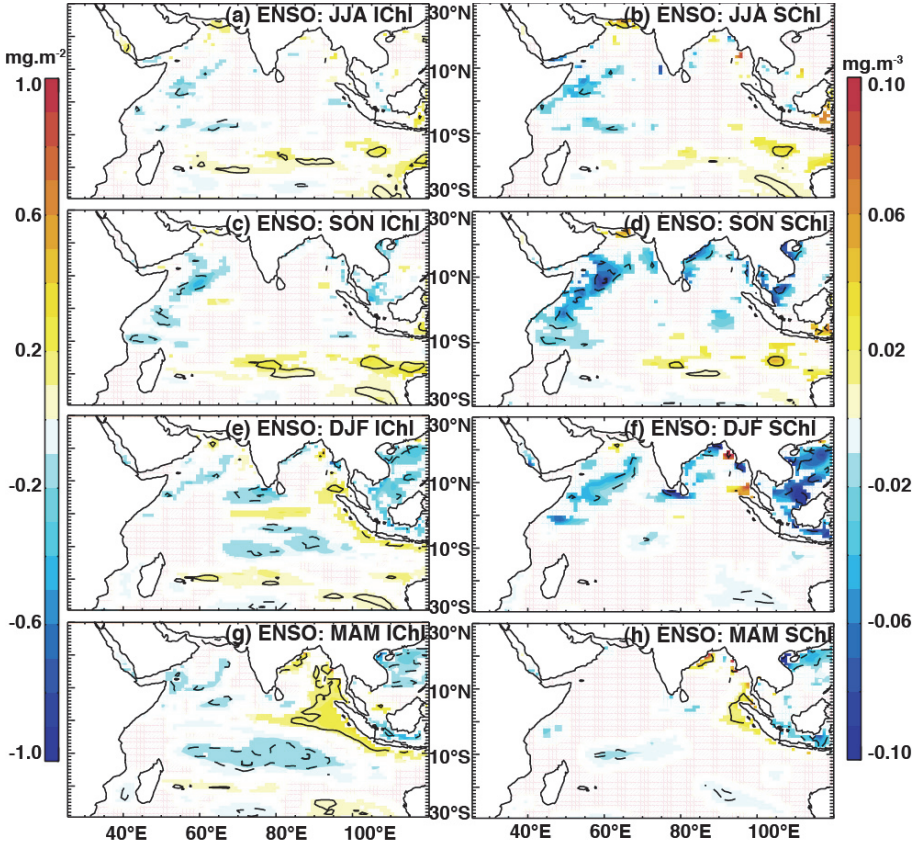

Fig. 8. Partial regression coefficients of de-seasoned anomalies of IChl (left panels) and SChl (right panels) as regressed onto the ENSO index, with the influence of IOD removed. Regression coefficients are computed for the 1961–2001 period and are shown when beyond a 90 % significance level. Thin, normal and thick contours indicate correlation coefficients of 0.4, 0.6 and 0.8, respectively. Plain (dashed) lines represent positive (negative) correlations.

BGD
10, 5841–5888, 2013

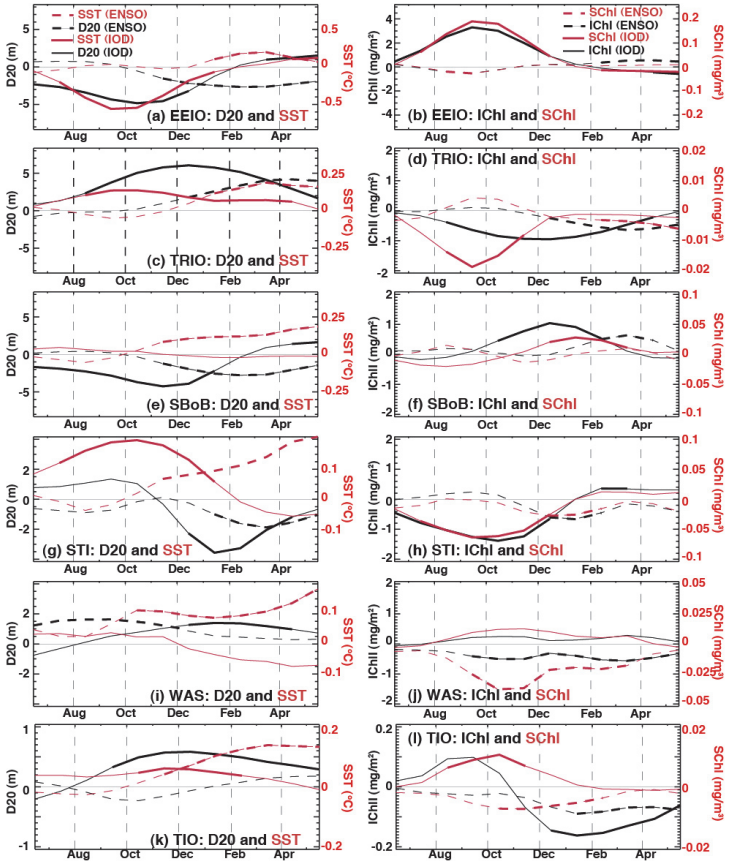

Fig. 9. Seasonal evolution of partial regression coefficients of D20 (black) and SST (red) anomalies on the left, and IChl (black) and SChl (red) anomalies on the right, as regressed onto IOD (plain) and ENSO (dashed) indices. The different geographical regions are indicated on Figs. 3 and 6 and described in Sect. 2.3. Bold line segments indicate when partial regression coefficients are above the 90 % significance level.

BGD
10, 5841–5888, 2013

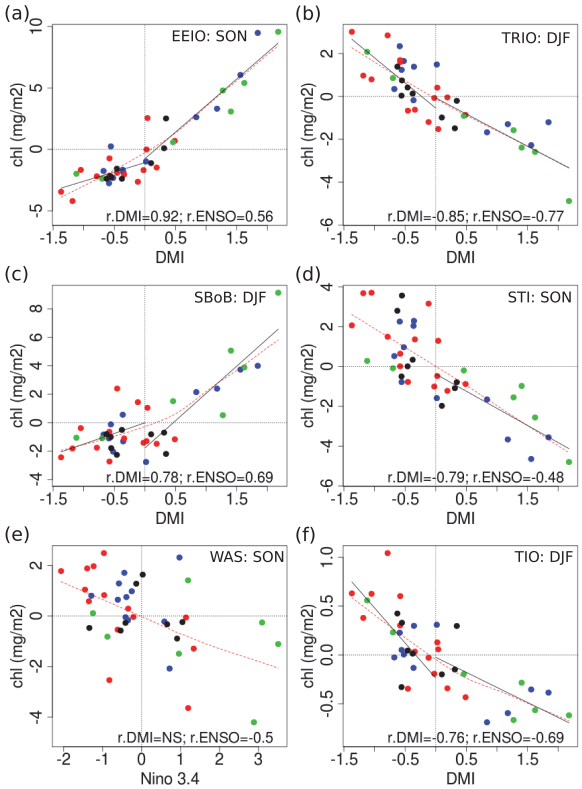

Fig. 10. Scatterplots of IChl anomalies, averaged over specified seasons and areas of interest, versus IOD and ENSO indices: **(a)** EEIO in SON, **(b)** TRIO in DJF, **(c)** SBoB in DJF, **(d)** STI in SON, **(e)** WAS in SON and **(f)** TIO in DJF. Pure IOD events in blue, pure ENSO events in red and co-occurring events in green, as identified by Meyers et al. (2007). Correlation coefficients for both climate indices are provided on the plot ($p < 0.05$; NS if $p \geq 0.05$). Solid black lines represent the slopes of significant least squares regressions, fit separately to index values > 0 and < 0 ($p < 0.05$). Red dotted line illustrates a Loess smooth curve fit by least squares.

BGD
10, 5841–5888, 2013